

# Controlled bond expansion for DMRG ground state search at single-site costs

Andreas Gleis,<sup>1</sup> Jheng-Wei Li,<sup>1</sup> and Jan von Delft<sup>1</sup>

<sup>1</sup>Arnold Sommerfeld Center for Theoretical Physics, Center for NanoScience, and Munich Center for Quantum Science and Technology, Ludwig-Maximilians-Universität München, 80333 Munich, Germany

(Dated: June 1, 2023)

DMRG ground state search algorithms employing symmetries must be able to expand virtual bond spaces by adding or changing symmetry sectors if these lower the energy. Traditional single-site DMRG does not allow bond expansion; two-site DMRG does, but at much higher computational costs. We present a controlled bond expansion (CBE) algorithm that yields two-site accuracy and convergence per sweep, at single-site costs. Given a matrix product state  $\Psi$  defining a variational space, CBE identifies parts of the orthogonal space carrying significant weight in  $H\Psi$  and expands bonds to include only these. CBE-DMRG uses no mixing parameters and is fully variational. Using CBE-DMRG, we show that the Kondo-Heisenberg model on a width 4 cylinder features two distinct phases differing in their Fermi surface volumes.

DOI:

*Introduction.* — A powerful tool for studying ground state properties of one- and two-dimensional quantum systems is the density matrix renormalization group (DMRG) [1–7]. Prominent two-dimensional applications include the  $t$ - $J$  [8–11] and Hubbard [12–18] models, and quantum magnets [19–22]. Due to their high numerical costs, such studies are currently limited to either small finite-sized systems or cylinders with small circumference. Progress towards computationally cheaper DMRG ground state search algorithms would clearly be welcome.

In this paper, we address this challenge. A DMRG ground state search explores a variational space spanned by matrix product states [23, 24]. If symmetries are exploited, the algorithm must be able to expand the auxiliary spaces associated with virtual bonds by adjusting symmetry sectors if this lowers the energy. Traditional single-site (1s) DMRG, which variationally updates one site at a time, does not allow such bond expansions. As a result, it often gets stuck in metastable configurations having quantum numbers different from the actual ground state. Two-site (2s) DMRG naturally leads to bond expansion, but carries much higher computational costs.

Hence, schemes have been proposed for achieving bond expansions at sub-2s costs, such as density matrix perturbation [25] or strictly single-site DMRG (DMRG3S) [26]. However, in these schemes, the degree of subspace expansion per local update is controlled by a heuristic mixing factor. Depending on its value, some subspace expansion updates increase, rather than decrease, the energy.

Here, we present a controlled bond expansion (CBE) algorithm which lowers the energy with each step and yields 2s accuracy and convergence per sweep, at 1s costs. Given a matrix product state  $\Psi$  defining a variational space, our key idea is to identify parts of the 2s orthogonal space that carry significant weight in  $H\Psi$ , and to include only these parts when expanding the virtual bonds of a 1s Hamiltonian. Remarkably, these parts can be found via a projector that can be constructed at 1s costs.

Using CBE-DMRG we study the Kondo-Heisenberg model on a width 4 cylinder and show that it features two phases differing in their Fermi surface volumes. We thereby further advance the understanding of this highly debated model using a controlled method.

*MPS basics.* — We briefly recall some standard MPS concepts [5], adopting the diagrammatic conventions of Ref. 27. Consider an  $\mathcal{L}$ -site system with an open boundary MPS wavefunction  $\Psi$  having dimensions  $d$  for physical sites and  $D$  for virtual bonds.  $\Psi$  can be written in bond-canonical form w.r.t. to any bond  $\ell$ ,

$$\Psi = \begin{array}{c} A_1 \quad A_2 \quad \dots \quad A_\ell \quad \Lambda_\ell \quad B_{\ell+1} \quad \dots \quad B_{\mathcal{L}-1} \quad B_{\mathcal{L}} \\ \begin{array}{ccccccc} \diagup & \diagdown & \dots & \diagdown & \circ & \diagup & \dots & \diagdown & \diagup \\ \diagdown & \diagup & \dots & \diagup & \diagdown & \diagdown & \dots & \diagdown & \diagdown \\ \diagdown & \diagdown & \dots & \diagdown & \diagdown & \diagdown & \dots & \diagdown & \diagdown \\ \diagdown & \diagdown & \dots & \diagdown & \diagdown & \diagdown & \dots & \diagdown & \diagdown \end{array} \end{array}. \quad (1)$$

The tensors  $\Lambda_\ell(\circ)$ ,  $A_\ell(\nabla)$  and  $B_\ell(\nabla)$  are variational parameters. They are linked by gauge relations,  $A_\ell \Lambda_\ell = \Lambda_{\ell-1} B_\ell$ , useful for shifting the bond tensor  $\Lambda_\ell$  to neighboring bonds.  $A_\ell$  and  $B_\ell$  are left and right-sided isometries, respectively, projecting  $Dd$ -dimensional *parent* ( $\rho$ ) spaces to  $D$ -dimensional *kept* ( $\kappa$ ) image spaces [27]; they satisfy

$$A_\ell^\dagger A_\ell = \begin{array}{c} A_\ell \\ \square \\ A_\ell^* \end{array} = \left( = \mathbb{1}_\kappa, \quad B_\ell B_\ell^\dagger = \begin{array}{c} B_\ell \\ \square \\ B_\ell^* \end{array} = \right) = \mathbb{1}_{\kappa_{\ell-1}}. \quad (2)$$

The Hamiltonian can similarly be expressed as a matrix product operator (MPO) with virtual bond dimension  $w$ ,

$$H = \begin{array}{c} W_1 \quad W_2 \quad \dots \quad W_\ell \quad W_{\ell+1} \quad \dots \quad W_{\mathcal{L}-1} \quad W_{\mathcal{L}} \\ \begin{array}{ccccccc} \diagup & \diagdown & \dots & \diagdown & \diagup & \dots & \diagdown & \diagup \\ \diagdown & \diagup & \dots & \diagup & \diagdown & \dots & \diagdown & \diagdown \\ \diagdown & \diagdown & \dots & \diagdown & \diagdown & \dots & \diagdown & \diagdown \\ \diagdown & \diagdown & \dots & \diagdown & \diagdown & \dots & \diagdown & \diagdown \end{array} \end{array}. \quad (3)$$

For 2s or 1s DMRG, the energy of  $\Psi$  is lowered by projecting  $H$  to a local variational space associated with sites  $(\ell, \ell+1)$  or  $\ell$ , respectively, and using its ground state (GS) within that space to locally update  $\Psi$ . The effective 2s and 1s Hamiltonians can be computed recursively using

$$H_\ell^{2s} = \begin{array}{c} D \\ \left[ \begin{array}{c} \diagup & \diagdown \\ \diagdown & \diagup \\ \diagdown & \diagdown \end{array} \right] \\ \ell-1 \quad \ell \quad \ell+1 \quad \ell+2 \end{array}^D = \begin{array}{c} \left[ \begin{array}{c} \diagup & \diagdown \\ \diagdown & \diagup \\ \diagdown & \diagdown \end{array} \right] \\ 1 \quad \ell-1 \quad \ell \quad \ell+1 \quad \ell+2 \end{array}, \quad (4a)$$

$$H_\ell^{1s} = \begin{array}{c} D \\ \left[ \begin{array}{c} \diagup \\ \diagdown \end{array} \right] \\ \ell-1 \quad \ell \quad \ell+1 \end{array}^D = \begin{array}{c} \left[ \begin{array}{c} \diagup \\ \diagdown \end{array} \right] \\ \ell-2 \quad \ell-1 \quad \ell \quad \ell+1 \end{array} = \begin{array}{c} \left[ \begin{array}{c} \diagup \\ \diagdown \end{array} \right] \\ \ell-1 \quad \ell \quad \ell+1 \quad \ell+2 \end{array}. \quad (4b)$$



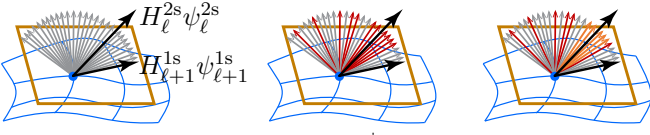


FIG. 2. The projection  $H_\ell^{2s}\psi_\ell^{2s} \xrightarrow{A_\ell^\dagger} H_{\ell+1}^{1s}\psi_{\ell+1}^{1s}$  to the tangent space (yellow) of the MPS manifold (blue) discards information from DD (depicted by grey arrows for DD basis vectors). *Relevant* information is recovered at 1s cost by constructing rDD through preselection (red), then final selection (orange).

truncation (*preselection*) truncates the central MPS bond from  $D \rightarrow D'$  (specified below) in the presence of its environment by minimizing the cost function  $\mathcal{C}_2$  (Fig. 1, bottom left); this replaces the full complement by a pre-selected complement,  $\bar{A}_\ell \nabla \rightarrow \hat{A}_\ell^{\text{pr}} \nabla$ , with reduced image dimension,  $\bar{D} \rightarrow \hat{D} = D'w$  [31]. The second truncation (*final selection*) minimizes the cost function  $\mathcal{C}_3$  (Fig. 1, bottom right) with central MPO bond closed as appropriate for  $H_\ell^{2s}\psi_\ell^{2s}$ : it further truncates  $\hat{A}_\ell^{\text{pr}}$  to yield the final truncated complement,  $\tilde{A}_\ell^{\text{tr}}, \nabla \rightarrow \nabla, \hat{D} \rightarrow \tilde{D} < D$ . To ensure 1s costs for final selection we need  $\tilde{D} = D$ , and thus choose  $D' = D/w$  for preselection.

*CBE update.*— A CBE update of bond  $\ell$  proceeds in four substeps. We describe them for a right-to-left sweep for building  $\tilde{A}_\ell^{\text{tr}}$  and updating  $C_{\ell+1}$  (left-to-right sweeps, building  $\tilde{B}_{\ell+1}^{\text{tr}}$  and updating  $C_\ell$ , are analogous).

(i) Compute  $\tilde{A}_\ell^{\text{tr}} (\nabla)$  using shrewd selection.

(ii) Expand bond  $\ell$  from dimension  $D$  to  $D + \tilde{D}$  by replacing  $A_\ell$  by an expanded isometry  $A_\ell^{\text{ex}}(\nabla) = A_\ell \oplus \tilde{A}_\ell^{\text{tr}}$ , and  $C_{\ell+1}$  by an expanded tensor initialized as  $C_{\ell+1}^{\text{ex},i} (\blacklozenge)$ , defined such that  $A_\ell^{\text{ex}} C_{\ell+1}^{\text{ex},i} = A_\ell C_{\ell+1}$ :

$$\frac{A_\ell}{d} \oplus \frac{\tilde{A}_\ell^{\text{tr}}}{d'} \frac{1}{\tilde{D}} = \frac{A_\ell^{\text{ex}}}{d} \frac{1}{(D+\tilde{D})} \frac{C_{\ell+1}^{\text{ex},i}}{d'} \frac{1}{D} = \left[ \text{Diagram} \right]_{\ell+1}. \quad (9)$$

Also construct an expanded *one-site* Hamiltonian, defined in a variational space of dimension  $D(D + \tilde{D})d$ :

$$H_{\ell+1}^{1s,\text{ex}} = \left[ \text{Diagram} \right]_{\ell+1} = \frac{D+\tilde{D}}{d} \left[ \text{Diagram} \right]_{\ell+1}^D. \quad (10)$$

(iii) Update  $C_{\ell+1}^{\text{ex}}$  variationally by using an iterative eigensolver, as usual in DMRG, to find the GS solution of  $(H_{\ell+1}^{1s,\text{ex}} - E)C_{\ell+1}^{\text{ex}} = 0$ , starting from  $C_{\ell+1}^{\text{ex},i}$ . (We employ a Lanczos eigensolver.) This has costs of  $\mathcal{O}(D^3 dw)$ . Thus,  $C_{\ell+1}^{\text{ex}}$  can be updated at 1s costs, while including only the most relevant 2s information via the contribution of  $\tilde{A}_\ell^{\text{tr}}$ .

(iv) Shift the isometry center from site  $\ell + 1$  to site  $\ell$  using a singular value decomposition (SVD) and truncate (*trim*) bond  $\ell$  from dimension  $D + \tilde{D}$  back to  $D$ , removing low-weight states. The discarded weight, say  $\xi$ , of this bond trimming serves as an error measure [29].

The energy minimization based on  $H_{\ell+1}^{1s,\text{ex}}$  is variational, hence each CBE update strictly lowers the GS energy. Though shrewd selection involves severe bond reductions,

it yields rDDs suitable for efficiently lowering the GS energy (in step (iii)). Moreover, although CBE explores a much smaller variational space than 2s DMRG, it converges at the same rate and accuracy (see below and Ref. [29]), since it focuses on the subspace that really matters for energy reduction. Section S-1 in [29] illustrates this by analysing singular value spectra. All in all, CBE is a 1s cost version of the 2s update, compatible with established DMRG parallelization schemes [45]. Similar to 2s [7], CBE can also be combined with mixing during the initial few sweeps (see Ref. 29, Sec. S-3).

We note that bond expansion using a truncated DD has been proposed before [26, 46]. But our  $A_\ell^{\text{ex}}(\nabla)$  outperforms that of DMRG3S [26] (see below and Ref. [29]); and we find  $A_\ell^{\text{ex}}(\nabla)$  at 1s costs, whereas Ref. 46 (on variational uniform MPS [47]) uses an SVD requiring 2s costs.

*Sweeping.*— Our computations exploit  $U(1)_{\text{ch}} \otimes \text{SU}(2)_{\text{sp}}$  charge and spin symmetries using QSpace [48, 49], with bond dimensions  $D^*$  (or  $D$ ) counting symmetry multiplets (or states). Usually,  $D^*$  is increased with each update during sweeping, from an initial  $D_1^*$  to a final  $D_f^* = \alpha D_1^*$ , with  $\alpha > 1$ . To achieve this with CBE we (i,ii) use  $D^* \simeq D_f^*/w^*$ ,  $\hat{D}^* = D_f^*$  (cf. Fig. 1) and expand from  $D_1^*$  to  $D_1^* + \hat{D}^* = D_f^*(1 + \delta)$ , (iii) call the iterative eigensolver, and (iv) truncate back to  $D_f^*$  when shifting the isometry center. We use  $\delta = 0.1$  for CBE, unless stated otherwise.

*Benchmarks.*— As a first benchmark, we consider the 1D Hubbard-Holstein (HH) model [32–36], described by

$$H_{\text{HH}} = - \sum_{\ell\sigma} (c_{\ell\sigma}^\dagger c_{\ell+1\sigma} + \text{h.c.}) + 0.8 \sum_{\ell} n_{\ell\uparrow} n_{\ell\downarrow} \quad (11)$$

$$+ 0.5 \sum_{\ell} b_{\ell}^\dagger b_{\ell} + \sqrt{0.2} \sum_{\ell} (n_{\ell\uparrow} + n_{\ell\downarrow} - 1) (b_{\ell}^\dagger + b_{\ell}).$$

Here,  $c_{\ell\sigma}^\dagger$  creates an electron and  $b_{\ell}^\dagger$  a phonon at site  $\ell$ , and  $n_{\ell\sigma} = c_{\ell\sigma}^\dagger c_{\ell\sigma}$ . We search for the GS with  $N = \mathcal{L} = 50$ , total spin  $S = 0$ , and restrict the maximum local number of excited phonons to  $N_{\text{ph}}^{\text{max}}$ . Then,  $d^*[d] = 3(N_{\text{ph}}^{\text{max}} + 1)[4(N_{\text{ph}}^{\text{max}} + 1)]$ . Figure 3(a) shows the relative error in energy vs. number of half-sweeps  $n_s$  for different  $D_{\text{max}}^*$  at fixed  $d^* = 12$ , comparing CBE and 2s DMRG schemes. The convergence with  $n_s$  is similar for CBE and 2s. Figure 3(b) compares the CPU time (measured on a single core of an Intel Core i7-9750H CPU) per sweep for CBE and 2s for different  $d^*$  at fixed  $D_{\text{max}}^*$ . Linear and quadratic fits confirm the expected  $d^*$  (1s) or  $d^{*2}$  (2s) scaling, respectively, highlighting the speedup from CBE.

Next, we consider  $\mathcal{L}_x \times \mathcal{L}_y = 10 \times 4$  and  $10 \times 6$  Hubbard cylinders (HC), described by (following Ref. 28)

$$H_{\text{HC}} = - \sum_{\langle \ell, \ell' \rangle, \sigma} (c_{\ell\sigma}^\dagger c_{\ell'\sigma} + \text{h.c.}) + 8 \sum_{\ell} n_{\ell\uparrow} n_{\ell\downarrow}. \quad (12)$$

Here,  $\ell = (x, y)$  is a 2D site index and  $\sum_{\langle \ell, \ell' \rangle}$  a nearest-neighbor sum. We search for the GS with total filling  $N = 0.9\mathcal{L}_x\mathcal{L}_y$  and spin  $S = 0$ . We use a real-space MPO,

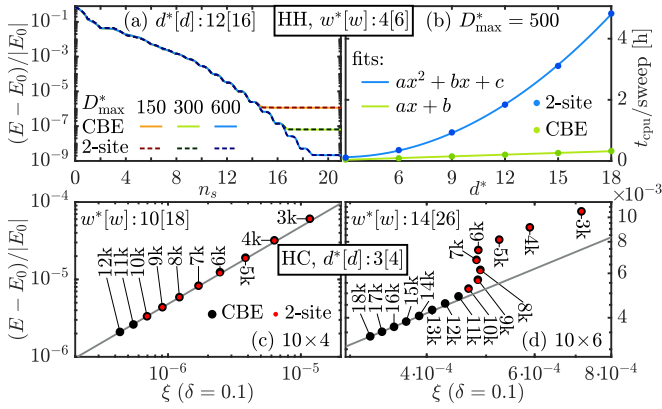


FIG. 3. Hubbard-Holstein (HH) model: (a) Convergence of the GS energy versus number of half-sweeps  $n_s$  at fixed  $d^* = 3(N_{\text{ph}}^{\text{max}} + 1)$ .  $E_0$  was obtained by linear  $\xi$ -extrapolation of data from  $D^*_{\text{max}} \in [1000, 1200]$ . (b) CPU time per sweep for various  $d^*$  at fixed  $D^*_{\text{max}}$ , showing  $d^*$  (CBE) vs.  $d^{*2}$  (2s) scaling. Hubbard cylinders (HC): Error in GS energy vs.  $\xi$  for (c)  $10 \times 4$  and (d)  $10 \times 6$  HCs, obtained with CBE (black) and 2s (red) DMRG, for various  $D^*_{\text{max}}$  (legends). Since 2s CPU times far exceed those of CBE, 2s data is only shown for  $D^*_{\text{max}} \leq 10k$ . Reference energies  $E_0 = -27.8816942$  ( $10 \times 4$ ) and  $-41.7474961$  ( $10 \times 6$ ) are obtained by linear  $\xi$ -extrapolation of the four most accurate CBE results to  $\xi = 0$  (grey line).

not the hybrid-space MPO [13, 50] used in Ref. 28. Figure 3(c,d) benchmarks CBE (black) against 2s DMRG (red); their accuracies match (same GS energy for given  $D^*$ ). CBE-DMRG yields controlled convergence for sufficiently large  $D^*$ , where the energy error decreases linearly with  $\xi$ . DMRG3S does not reach 2s accuracy for this model, as is clear from the data shown in Ref. 28 Sec. V E.

Further benchmarks and comparison to DMRG3S are shown in Ref. 29, Secs. S-2,3. We find that CBE has similar run time per sweep but converges faster than DMRG3S [26]: for given  $D^*_{\text{max}}$ , the energy converges in fewer sweeps and less run time, and reaches a lower value.

*Kondo-Heisenberg cylinders.*— Finally, to include some new physics results in this paper, we study the Kondo-Heisenberg (KH) lattice model on a cylinder. The KH model is believed to describe the essential physics of heavy-fermion (HF) materials [37, 51–53], which feature many interesting phenomena. One of the most intriguing is the so-called Kondo breakdown (KB) quantum critical point (QCP) [39, 43, 54], where collective Kondo singlets [43] formed at strong coupling break up, leading to a FS reconstruction [55–58] at  $T = 0$ . Strange metal behaviour is observed at finite temperatures with e.g.  $\sim T$  resistivity [58–62] or  $\sim T \log T$  specific heat [61–64].

Theoretical understanding of the KB-QCP is still incomplete, in part due to scarceness of numerical simulations. Prior numerical studies used dynamical mean-field theory [65–69] and Monte Carlo methods [70–73], but we are not aware of DMRG results on the KB-QCP. Here, we take first steps in this direction by studying FS reconstruction on a KH cylinder: we show that at  $T = 0$ , there

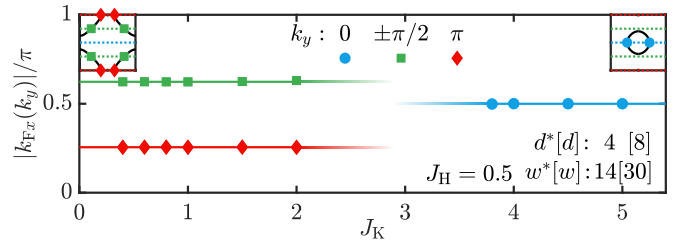


FIG. 4. Kondo-Heisenberg (KH) cylinder: Fermi wavevectors  $|k_{\text{Fx}}(k_y)|$  for a  $40 \times 4$  KH cylinder for various values of  $J_K$ . Symbols are data points (error bars are below symbol size), lines are guides to the eye. In the insets, black lines sketch the presumed FS for  $\mathcal{L}_y \rightarrow \infty$ , dotted lines show the  $k_y$  values allowed for  $\mathcal{L}_y = 4$ .

are two distinct phases featuring different Fermi surfaces.

We study a  $\mathcal{L}_x \times \mathcal{L}_y = 40 \times 4$  KH cylinder, described by

$$H_{\text{KH}} = - \sum_{\langle \ell, \ell' \rangle, \sigma} (c_{\ell\sigma}^\dagger c_{\ell'\sigma} + \text{h.c.}) + J_K \sum_{\ell} \mathbf{S}_{\ell} \cdot \mathbf{s}_{\ell} + \frac{1}{2} \sum_{\langle \ell, \ell' \rangle} \mathbf{S}_{\ell} \cdot \mathbf{S}_{\ell'}.$$

Here,  $\mathbf{s}_{\ell} = \frac{1}{2} \sum_{\sigma\sigma'} c_{\ell\sigma}^\dagger \boldsymbol{\sigma}_{\sigma\sigma'} c_{\ell\sigma'}$  and  $\mathbf{S}_{\ell}$  are electron and local moment spin- $\frac{1}{2}$  operators at site  $\ell$ . We search for the GS with total filling  $N = 1.25 \mathcal{L}_x \mathcal{L}_y$  and spin  $S = 0$ .

For a  $\mathcal{L}_y = 4$  cylinder, the Brillouin zone consists of four lines, since  $k_y \in \{0, \pm \frac{\pi}{2}, \pi\}$  is discrete. If such a line cuts the  $\mathcal{L}_y \rightarrow \infty$  FS, that defines a ‘‘Fermi point’’, with Fermi momentum  $(k_{\text{Fx}}(k_y), k_y)$ . We have extracted the corresponding  $k_{\text{Fx}}(k_y)$  values from CBE-DMRG results for the single-particle density matrix (see Ref. 29, Sec. S-4 B for details; Fig. S-13 shows controlled convergence of this quantity). Figure 4 shows the results for various values of  $J_K$ . There are clearly two distinct phases with qualitatively different Fermi points  $k_{\text{Fx}}(k_y)$ . At small  $J_K \leq 2$ , we find Fermi points at  $(|k_{\text{Fx}}|, |k_y|) = (0.625\pi, \frac{\pi}{2})$  and  $(0.256\pi, \pi)$ , matching the free-electron values at  $J_K = 0$ . By contrast, at large  $J_K \geq 2.8$ , we find Fermi points only at  $(\frac{\pi}{2}, 0)$ , suggesting a FS reconstruction at some  $J_{\text{Kc}}$  in between. Note also that  $k_{\text{Fx}}(k_y)$  remains  $J_K$ -independent in each of the two regimes. This is expected from Luttinger’s sum rule [40, 42], which links the effective number  $n_{\text{eff}}$  of mobile charge carriers (defined modulo 2, i.e. up to filled bands) to the FS volume (see Ref. 29, Sec. S-4 C for details). For small  $J_K \leq 0.75$ , we find  $n_{\text{eff}} = 1.25$ , consistent with 25% electron doping. By contrast, at large  $J_K \geq 2.8$  we find  $n_{\text{eff}} = 0.25 = 2.25 \bmod 2$ , consistent with the spins becoming mobile charge carriers by ‘‘binding’’ to the electrons [43]. Pinpointing and studying a possible KB-QCP separating the two phases is left for future work.

*Summary and outlook.*— CBE expands bonds by adding subspaces on which  $\Delta_E^{2s}$ , the 2s contribution to the energy variance, has significant weight, thus making these subspaces accessible to 1s energy minimization. CBE is fully variational and has 1s costs, since the variational space is only slightly expanded relative to 1s DMRG.

By significantly saving costs, CBE opens the door to studying challenging models of current interest at higher accuracy (larger  $D$ ) than previously possible, or tackling



more complex models, with  $d$  or  $w$  so large that they were hitherto out of reach. Examples are multi-band models with several different type of couplings, in particular in two-dimensional settings, models involving bosonic excitations, and quantum-chemical applications. We have made a first step in this direction by showing that the KH model on a width 4 cylinder features two phases with distinct FS volumes. Our study of the KH model opens the door to investigate this model in more depth; for example, follow-up work may aim to sort out the range of applicability of existing approximate approaches, e.g. parton mean-field theories [74, 75] or DMFT based studies [65–69].

More generally, CBE can be used for any variational MPS optimization task. Besides energy minimization, an example is approximating a given  $\Psi$  by a  $\Psi'$  with smaller bond dimension through minimization of  $\|\Psi' - \Psi\|$ . CBE can also be used to build Krylov spaces with 2s accuracy at 1s costs, relevant for all of the many MPS methods relying on Krylov methods. For example, in a follow-up paper [76] we focus on MPS time evolution using the time-dependent variational principle (TDVP), and use CBE to achieve dramatic improvements in performance. Finally, analogous statements hold for variational optimization or time evolution of MPOs. Thus, CBE will become a widely-used, indispensable tool in the MPS/MPO toolbox.

We thank A. Weichselbaum for inspiring discussions and S.-S.B. Lee, J. Espinoza, M. Lotem, J. Shim and A. Weichselbaum for comments on our manuscript. This work was funded in part by the Deutsche Forschungsgemeinschaft under Germany's Excellence Strategy EXC-2111 (Project No. 390814868). It is part of the Munich Quantum Valley, supported by the Bavarian state government with funds from the Hightech Agenda Bayern Plus.

- 
- [1] S. R. White, Density matrix formulation for quantum renormalization groups, *Phys. Rev. Lett.* **69**, 2863 (1992).
- [2] S. R. White, Density-matrix algorithms for quantum renormalization groups, *Phys. Rev. B* **48**, 10345 (1993).
- [3] F. Verstraete, D. Porras, and J. I. Cirac, Density matrix renormalization group and periodic boundary conditions: A quantum information perspective, *Phys. Rev. Lett.* **93**, 227205 (2004).
- [4] U. Schollwöck, The density-matrix renormalization group, *Rev. Mod. Phys.* **77**, 259 (2005).
- [5] U. Schollwöck, The density-matrix renormalization group in the age of matrix product states, *Annals of Physics* **326**, 96 (2011).
- [6] S. R. White, Spin gaps in a frustrated Heisenberg model for  $\text{cav}_4\text{o}_9$ , *Phys. Rev. Lett.* **77**, 3633 (1996).
- [7] E. Stoudenmire and S. R. White, Studying two-dimensional systems with the density matrix renormalization group, *Ann. Rev. Cond. Mat. Phys.* **3**, 111 (2012).
- [8] S. R. White and D. J. Scalapino, Density matrix renormalization group study of the striped phase in the 2d  $t - J$  model, *Phys. Rev. Lett.* **80**, 1272 (1998).
- [9] S. R. White and D. J. Scalapino, Checkerboard patterns in the  $t - J$  model, *Phys. Rev. B* **70**, 220506 (2004).
- [10] S. R. White and D. J. Scalapino, Pairing on striped  $t - t' - J$  lattices, *Phys. Rev. B* **79**, 220504 (2009).
- [11] S. Jiang, D. J. Scalapino, and S. R. White, Ground-state phase diagram of the  $t - t' - J$  model, *Proceedings of the National Academy of Sciences* **118**, e2109978118 (2021).
- [12] J. P. F. LeBlanc, A. E. Antipov, F. Becca, I. W. Bulik, G. K.-L. Chan, C.-M. Chung, Y. Deng, M. Ferrero, T. M. Henderson, C. A. Jiménez-Hoyos, E. Kozik, X.-W. Liu, A. J. Millis, N. V. Prokof'ev, M. Qin, G. E. Scuseria, H. Shi, B. V. Svistunov, L. F. Tocchio, I. S. Tupitsyn, S. R. White, S. Zhang, B.-X. Zheng, Z. Zhu, and E. Gull (Simons Collaboration on the Many-Electron Problem), Solutions of the two-dimensional Hubbard model: Benchmarks and results from a wide range of numerical algorithms, *Phys. Rev. X* **5**, 041041 (2015).
- [13] G. Ehlers, S. R. White, and R. M. Noack, Hybrid-space density matrix renormalization group study of the doped two-dimensional Hubbard model, *Phys. Rev. B* **95**, 125125 (2017).
- [14] B.-X. Zheng, C.-M. Chung, P. Corboz, G. Ehlers, M.-P. Qin, R. M. Noack, H. Shi, S. R. White, S. Zhang, and G. K.-L. Chan, Stripe order in the underdoped region of the two-dimensional Hubbard model, *Science* **358**, 1155 (2017).
- [15] E. W. Huang, C. B. Mendl, H.-C. Jiang, B. Moritz, and T. P. Devereaux, Stripe order from the perspective of the Hubbard model, *npj Quantum Materials* **3**, 22 (2018).
- [16] M. Qin, C.-M. Chung, H. Shi, E. Vitali, C. Hubig, U. Schollwöck, S. R. White, and S. Zhang (Simons Collaboration on the Many-Electron Problem), Absence of superconductivity in the pure two-dimensional Hubbard model, *Phys. Rev. X* **10**, 031016 (2020).
- [17] Y.-F. Jiang, J. Zaanen, T. P. Devereaux, and H.-C. Jiang, Ground state phase diagram of the doped Hubbard model on the four-leg cylinder, *Phys. Rev. Research* **2**, 033073 (2020).
- [18] H.-C. Jiang and S. A. Kivelson, Stripe order enhanced superconductivity in the Hubbard model, *PNAS* **119**, e2109406119 (2022).
- [19] S. Yan, D. A. Huse, and S. R. White, Spin-liquid ground state of the  $S = 1/2$  kagome Heisenberg antiferromagnet, *Science* **332**, 1173 (2011).
- [20] S. Depenbrock, I. P. McCulloch, and U. Schollwöck, Nature of the spin-liquid ground state of the  $S = 1/2$  Heisenberg model on the kagome lattice, *Phys. Rev. Lett.* **109**, 067201 (2012).
- [21] F. Kolley, S. Depenbrock, I. P. McCulloch, U. Schollwöck, and V. Alba, Phase diagram of the  $J_1 - J_2$  Heisenberg model on the kagome lattice, *Phys. Rev. B* **91**, 104418 (2015).
- [22] Y.-C. He, M. P. Zaletel, M. Oshikawa, and F. Pollmann, Signatures of Dirac cones in a DMRG study of the kagome Heisenberg model, *Phys. Rev. X* **7**, 031020 (2017).
- [23] S. Östlund and S. Rommer, Thermodynamic limit of density matrix renormalization, *Phys. Rev. Lett.* **75**, 3537 (1995).
- [24] S. Rommer and S. Östlund, Class of ansatz wave functions for one-dimensional spin systems and their relation to the density matrix renormalization group, *Phys. Rev. B* **55**, 2164 (1997).
- [25] S. R. White, Density matrix renormalization group algorithms with a single center site, *Phys. Rev. B* **72**, 180403 (2005).

- [26] C. Hubig, I. P. McCulloch, U. Schollwöck, and F. A. Wolf, Strictly single-site DMRG algorithm with subspace expansion, *Phys. Rev. B* **91**, 155115 (2015).
- [27] A. Gleis, J.-W. Li, and J. von Delft, Projector formalism for kept and discarded spaces of matrix product states, *Phys. Rev. B* **106**, 195138 (2022).
- [28] C. Hubig, J. Haegeman, and U. Schollwöck, Error estimates for extrapolations with matrix-product states, *Phys. Rev. B* **97**, 045125 (2018).
- [29] See Supplemental Material at [url] for a detailed analysis of shrewd selection; a pseudocode for shrewd selection; additional simple benchmarks; a comparison to DMRG3S; and more details on the analysis of the Kondo-Heisenberg model on a 4-leg cylinder. The Supplemental Material includes Refs. [32–44].
- [30] If 2s DMRG has converged to an optimal MPS  $\Psi_D$  with fixed bond dimension  $D$ , the size of rDD is zero. Because  $\Psi_D$  is already optimal (at fixed  $D$ ), any state in DD is less relevant than those already present in the kept space of  $\Psi_D$ . As a result,  $\Psi_D$  cannot be further optimized unless  $D$  is increased. Away from convergence, the size of rDD is usually still much smaller than the already somewhat optimized kept space, which in turn is much smaller than DD. Expanding by rDD (CBE) instead of DD (2s) is similar in spirit to using an iterative eigensolver for Eq. (5) instead of full diagonalization.
- [31] We could achieve the desired reduction  $\bar{D} \rightarrow \tilde{D}$  already during preselection by choosing  $D' = \tilde{D}/w$  there, so that  $\hat{D} = \tilde{D}$ ; however, that would neglect the information that in  $H^{2s}\psi^{2s}$  the central MPO bond is closed. Final selection serves to include that information.
- [32] E. Jeckelmann and S. R. White, Density-matrix renormalization-group study of the polaron problem in the Holstein model, *Phys. Rev. B* **57**, 6376 (1998).
- [33] M. Tezuka, R. Arita, and H. Aoki, Phase diagram for the one-dimensional Hubbard-Holstein model: A density-matrix renormalization group study, *Phys. Rev. B* **76**, 155114 (2007).
- [34] H. Fehske, G. Hager, and E. Jeckelmann, Metallicity in the half-filled Holstein-Hubbard model, *E. J. Phys.* **84**, 57001 (2008).
- [35] S. Ejima and H. Fehske, DMRG analysis of the sdw-cdw crossover region in the 1d half-filled Hubbard-Holstein model, *J. Phys.: Conference Series* **200**, 012031 (2010).
- [36] T. E. Reinhard, U. Mordovina, C. Hubig, J. S. Kretschmer, U. Schollwöck, H. Appel, M. A. Sentef, and A. Rubio, Density-matrix embedding theory study of the one-dimensional Hubbard-Holstein model, *J. Chem. Theory and Comp.* **15**, 2221 (2019).
- [37] P. Coleman, Heavy fermions: Electrons at the edge of magnetism, in *Handbook of Magnetism and Advanced Magnetic Materials*, Vol. 1, edited by H. Kronmüller and S. Parkin (Wiley, 2007) pp. 95–148.
- [38] M. Ye, H.-H. Kung, P. F. S. Rosa, E. D. Bauer, K. Haule, and G. Blumberg, Anisotropy of Kondo-lattice coherence in momentum space for CeCoIn<sub>5</sub>, arXiv:2202.09642 [cond-mat.str-el] (2022).
- [39] P. Coleman, C. Pépin, Q. Si, and R. Ramazashvili, How do Fermi liquids get heavy and die?, *J. Phys. Cond. Mat.* **13**, R723 (2001).
- [40] J. M. Luttinger, Fermi surface and some simple equilibrium properties of a system of interacting fermions, *Phys. Rev.* **119**, 1153 (1960).
- [41] D. Sénéchal, An introduction to bosonization 10.48550/arxiv.cond-mat/9908262 (1999).
- [42] M. Oshikawa, Topological approach to Luttinger’s theorem and the Fermi surface of a Kondo lattice, *Phys. Rev. Lett.* **84**, 3370 (2000).
- [43] Q. Si, J. H. Pixley, E. Nica, S. J. Yamamoto, P. Goswami, R. Yu, and S. Kirchner, Kondo destruction and quantum criticality in Kondo lattice systems, *Journal of the Physical Society of Japan* **83**, 061005 (2014).
- [44] Y. Nishikawa, O. J. Curtin, A. C. Hewson, and D. J. G. Crow, Magnetic field induced quantum criticality and the Luttinger sum rule, *Phys. Rev. B* **98**, 104419 (2018).
- [45] E. M. Stoudenmire and S. R. White, Real-space parallel density matrix renormalization group, *Phys. Rev. B* **87**, 155137 (2013).
- [46] V. Zauner-Stauber, L. Vanderstraeten, M. T. Fishman, F. Verstraete, and J. Haegeman, Variational optimization algorithms for uniform matrix product states, *Phys. Rev. B* **97**, 045145 (2018).
- [47] L. Vanderstraeten, J. Haegeman, and F. Verstraete, Tangent-space methods for uniform matrix product states, *SciPost Phys. Lect. Notes* **7** (2019).
- [48] A. Weichselbaum, Non-abelian symmetries in tensor networks: A quantum symmetry space approach, *Ann. of Phys.* **327**, 2972 (2012).
- [49] A. Weichselbaum, X-symbols for non-abelian symmetries in tensor networks, *Phys. Rev. Research* **2**, 023385 (2020).
- [50] J. Motruk, M. P. Zaletel, R. S. K. Mong, and F. Pollmann, Density matrix renormalization group on a cylinder in mixed real and momentum space, *Phys. Rev. B* **93**, 155139 (2016).
- [51] S. Kirchner, S. Paschen, Q. Chen, S. Wirth, D. Feng, J. D. Thompson, and Q. Si, Colloquium: Heavy-electron quantum criticality and single-particle spectroscopy, *Rev. Mod. Phys.* **92**, 011002 (2020).
- [52] H. v. Löhneysen, A. Rosch, M. Vojta, and P. Wölfle, Fermi-liquid instabilities at magnetic quantum phase transitions, *Rev. Mod. Phys.* **79**, 1015 (2007).
- [53] G. R. Stewart, Non-Fermi-liquid behavior in  $d$ - and  $f$ -electron metals, *Rev. Mod. Phys.* **73**, 797 (2001).
- [54] P. Coleman and C. Pépin, What is the fate of the heavy electron at a quantum critical point?, *Physica B: Condensed Matter* **312-313**, 383 (2002), the International Conference on Strongly Correlated Electron Systems.
- [55] S. Paschen, T. Lühmann, S. Wirth, P. Gegenwart, O. Trovarelli, C. Geibel, F. Steglich, P. Coleman, and Q. Si, Hall-effect evolution across a heavy-fermion quantum critical point, *Nature* **432**, 881 (2004).
- [56] H. Shishido, R. Settai, H. Harima, and Y. Ōnuki, A drastic change of the Fermi surface at a critical pressure in CeRhIn<sub>5</sub>: dhva study under pressure, *Journal of the Physical Society of Japan* **74**, 1103 (2005), <https://doi.org/10.1143/JPSJ.74.1103>.
- [57] S. Friedemann, N. Oeschler, S. Wirth, C. Krellner, C. Geibel, F. Steglich, S. Paschen, S. Kirchner, and Q. Si, Fermi-surface collapse and dynamical scaling near a quantum-critical point, *Proc. Natl. Acad. Sci.* **107**, 14547 (2010).
- [58] N. Maksimovic, D. H. Eilbott, T. Cookmeyer, F. Wan, J. Ruzs, V. Nagarajan, S. C. Haley, E. Maniv, A. Gong, S. Faubel, I. M. Hayes, A. Bangura, J. Singleton, J. C. Palmstrom, L. Winter, R. McDonald, S. Jang, P. Ai, Y. Lin, S. Ciocys, J. Gobbo, Y. Werman, P. M. Oppeneer, E. Altman, A. Lanzara, and J. G. Analytis, Evidence

- for a delocalization quantum phase transition without symmetry breaking in CeCoIn<sub>5</sub>, *Science* **375**, 76 (2022).
- [59] V. Martelli, A. Cai, E. M. Nica, M. Taupin, A. Prokofiev, C.-C. Liu, H.-H. Lai, R. Yu, K. Ingersent, R. K uchler, A. M. Strydom, D. Geiger, J. Haenel, J. Larrea, Q. Si, and S. Paschen, Sequential localization of a complex electron fluid, *Proceedings of the National Academy of Sciences* **116**, 17701 (2019).
- [60] L. Prochaska, X. Li, D. C. MacFarland, A. M. Andrews, M. Bonta, E. F. Bianco, S. Yazdi, W. Schrenk, H. Detz, A. Limbeck, Q. Si, E. Ringe, G. Strasser, J. Kono, and S. Paschen, Singular charge fluctuations at a magnetic quantum critical point, *Science* **367**, 285 (2020).
- [61] O. Trovarelli, C. Geibel, S. Mederle, C. Langhammer, F. M. Grosche, P. Gegenwart, M. Lang, G. Sparn, and F. Steglich, YbRh<sub>2</sub>Si<sub>2</sub>: Pronounced non-Fermi-liquid effects above a low-lying magnetic phase transition, *Phys. Rev. Lett.* **85**, 626 (2000).
- [62] H. Zhao, J. Zhang, M. Lyu, S. Bachus, Y. Tokiwa, P. Gegenwart, S. Zhang, J. Cheng, Y.-f. Yang, G. Chen, Y. Isikawa, Q. Si, F. Steglich, and P. Sun, Quantum-critical phase from frustrated magnetism in a strongly correlated metal, *Nature Phys.* **15**, 1261 (2019).
- [63] H. L ohneysen, M. Sieck, O. Stockert, and M. Waffenschmidt, Investigation of non-fermi-liquid behavior in CeCu<sub>6-x</sub>Au<sub>x</sub>, *Physica B: Condensed Matter* **223-224**, 471 (1996), proceedings of the International Conference on Strongly Correlated Electron Systems.
- [64] H. von L ohneysen, Non-fermi-liquid behaviour in the heavy-fermion system, *Journal of Physics: Condensed Matter* **8**, 9689 (1996).
- [65] L. De Leo, M. Civelli, and G. Kotliar, Cellular dynamical mean-field theory of the periodic Anderson model, *Phys. Rev. B* **77**, 075107 (2008).
- [66] L. De Leo, M. Civelli, and G. Kotliar,  $T = 0$  heavy-fermion quantum critical point as an orbital-selective Mott transition, *Phys. Rev. Lett.* **101**, 256404 (2008).
- [67] D. Tanaskovi c, K. Haule, G. Kotliar, and V. Dobrosavljevi c, Phase diagram, energy scales, and nonlocal correlations in the Anderson lattice model, *Phys. Rev. B* **84**, 115105 (2011).
- [68] Q. Si, S. Rabello, K. Ingersent, and J. L. Smith, Locally critical quantum phase transitions in strongly correlated metals, *Nature* **413**, 804 (2001).
- [69] Q. Si, S. Rabello, K. Ingersent, and J. L. Smith, Local fluctuations in quantum critical metals, *Phys. Rev. B* **68**, 115103 (2003).
- [70] F. F. Assaad, Quantum monte carlo simulations of the half-filled two-dimensional Kondo lattice model, *Phys. Rev. Lett.* **83**, 796 (1999).
- [71] S. Capponi and F. F. Assaad, Spin and charge dynamics of the ferromagnetic and antiferromagnetic two-dimensional half-filled Kondo lattice model, *Phys. Rev. B* **63**, 155114 (2001).
- [72] F. Parisen Toldin, T. Sato, and F. F. Assaad, Mutual information in heavy-fermion systems, *Phys. Rev. B* **99**, 155158 (2019).
- [73] B. Danu, Z. Liu, F. F. Assaad, and M. Raczkowski, Zooming in on heavy fermions in Kondo lattice models, *Phys. Rev. B* **104**, 155128 (2021).
- [74] T. Senthil, S. Sachdev, and M. Vojta, Fractionalized fermi liquids, *Phys. Rev. Lett.* **90**, 216403 (2003).
- [75] T. Senthil, M. Vojta, and S. Sachdev, Weak magnetism and non-fermi liquids near heavy-fermion critical points, *Phys. Rev. B* **69**, 035111 (2004).
- [76] J.-W. Li, A. Gleis, and J. von Delft, Time-dependent variational principle with controlled bond expansion for matrix product states, [arXiv:2208.10972](https://arxiv.org/abs/2208.10972) [cond-mat.str-el] (2022).

# Supplemental material: Controlled bond expansion for DMRG ground state search at single-site costs

Andreas Gleis,<sup>1</sup> Jheng-Wei Li,<sup>1</sup> and Jan von Delft<sup>1</sup>

<sup>1</sup>*Arnold Sommerfeld Center for Theoretical Physics, Center for NanoScience, and Munich Center for Quantum Science and Technology, Ludwig-Maximilians-Universität München, 80333 Munich, Germany*

(Dated: June 1, 2023)

This supplement offers additional material on five issues: in Sec. S-1, details on the implementation of shrewd selection, including pseudocode, and a detailed analysis of preselection and final selection; in Sec. S-2, a simple additional benchmark of CBE-DMRG on free Fermions; in Sec. S-3, a comparison to DMRG3S; and in Sec. S-4, more details on the analysis of the Kondo-Heisenberg model on a 4-leg cylinder.

## S-1. SHREWD SELECTION

Figures 1 and 2 in the main text introduce a novel scheme needed for CBE, called *shrewd selection*. In this section, we discuss it in detail. Section S-1 A provides algorithmic details; Sec. S-1 B discusses various options for choosing the parameters involved in preselection and final selection; Secs. S-1 C and S-1 D discusses the properties of the singular values and singular vectors obtained; and

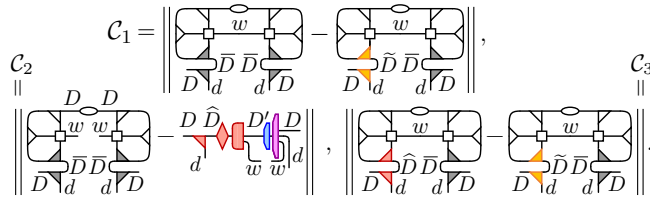


FIG. S-1. Shrewd selection (concept). During a right-to-left CBE sweep, bond  $\ell$  is expanded from  $A_\ell(\nabla)$  to  $A_\ell \oplus \tilde{A}_\ell^{\text{tr}}(\nabla \oplus \nabla)$ , where  $\tilde{A}_\ell^{\text{tr}}(\nabla)$ , with image dimension  $\tilde{D}$ , is a truncation of  $\tilde{A}_\ell(\nabla)$ , with image dimension  $\tilde{D} = D(d-1)$ . This expansion will reduce  $\Delta_E^{2s}$  significantly if  $\tilde{A}_\ell^{\text{tr}} \oplus \tilde{B}_{\ell+1}(\nabla \otimes \nabla)$  targets rDD, a  $\tilde{D}\tilde{D}$ -dimensional subspace of the  $\tilde{D}^2$ -dimensional space  $\tilde{D}\tilde{D}$  on which  $H_\ell^{2s} \psi_\ell^{2s}$  has significant weight. As explained in the main text, ideally,  $\tilde{A}_\ell^{\text{tr}}(\nabla)$  should minimize the cost function  $C_1$ . To achieve this at 1s costs, we instead find  $\tilde{A}_\ell^{\text{tr}}(\nabla)$  using shrewd selection, involving two separate truncations. The first truncation (*preselection*) truncates the central MPS bond from  $D \rightarrow D'$  in the presence of its environment by minimizing  $C_2$ ; this replaces the full complement by a preselected complement,  $\tilde{A}_\ell \nabla \rightarrow \tilde{A}_\ell^{\text{pr}} \nabla$ , with reduced image dimension,  $\tilde{D} \rightarrow \tilde{D} = D'w$  [31]. The second truncation (*final selection*) minimizes  $C_3$  with central MPO bond closed as appropriate for  $H_\ell^{2s} \psi_\ell^{2s}$ : it further truncates  $\tilde{A}_\ell^{\text{pr}}$  to yield the final truncated complement,  $\tilde{A}_\ell^{\text{tr}}, \nabla \rightarrow \tilde{\nabla}$ ,  $\tilde{D} \rightarrow \tilde{D} < D$ . To ensure 1s costs for final selection we need  $\tilde{D} = D$ , and thus choose  $D' = D/w$  for preselection. The truncations underlying preselection and final selection are explained in detail in Fig. S-2.

Sec. S-1 E discusses the convergence rate per sweep.

## A. Algorithmic details

For convenience, Fig. 1 of the main text is shown again in Fig. S-1, with a caption summarizing the main ideas underlying shrewd selection. Its two ingredients, preselection and final selection, are explained in detail in Fig. S-2 using tensor network diagrams. Table I provides pseudocode for the tensor network diagrams in Fig. S-2.

In the remainder of this section we discuss preselection and final selection in more detail, and illustrate their effects on the properties of various singular value spectra

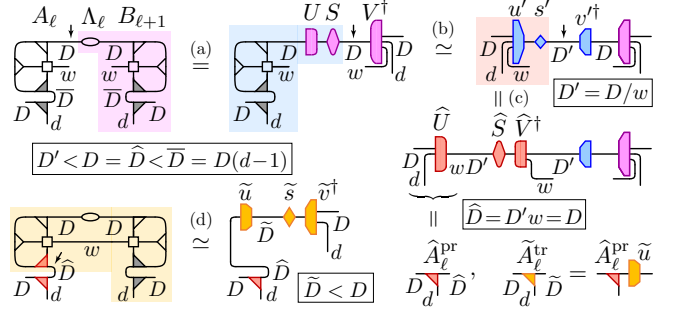


FIG. S-2. Shrewd selection (details). Computation of (a-c) the preselected complement  $\hat{A}_\ell^{\text{pr}}(\nabla)$  to minimize  $C_2$ , and (d) the final truncated complement  $\tilde{A}_\ell^{\text{tr}}(\nabla)$  to minimize  $C_3$ , using four SVDs, all with at most 1s costs. For each, an arrow indicates a bond being opened before doing the SVD, shading and symbols in matching colors indicate the SVD input and output, and the latter is written as  $USV^\dagger$  or  $usv^\dagger$  when involving no or some truncation, respectively. Importantly, we express  $\tilde{A}_\ell \tilde{A}_\ell^\dagger$  and  $\tilde{B}_{\ell+1}^\dagger \tilde{B}_{\ell+1}$  (grey) as  $\mathbb{1}_\ell^p - A_\ell A_\ell^\dagger$  and  $\mathbb{1}_{\ell+1}^p - B_{\ell+1}^\dagger B_{\ell+1}$  (Eq. (7b)), avoiding the computation of  $\tilde{A}_\ell$  and  $\tilde{B}_{\ell+1}$ . (a) The first SVD canonicalizes the right side of the diagram, assigning its weights to the central MPS bond. (b) The second SVD and truncation reduces the dimension of this bond,  $D \rightarrow D' = D/w$ . (c) The third SVD regrouping indices to combine the truncated MPS bond and the MPO bond into a composite bond of dimension  $\hat{D} = D'w = D$ , yielding the preselected complement  $\hat{A}_\ell^{\text{pr}} = \hat{U}(\nabla)$ . Nominally, step (c) would require no truncation if exact arithmetic were used, but in practice (numerically) zero singular values, of order  $\mathcal{O}(10^{-16})$ , may arise; these must be discarded to ensure  $A_\ell^\dagger \hat{A}_\ell^{\text{pr}} = 0$ . (d) The fourth SVD and truncation yields the final truncated complement  $\tilde{A}_\ell^{\text{tr}} = \hat{A}_\ell^{\text{pr}} \tilde{u}(\nabla)$ , with bond reduction  $\hat{D} \rightarrow \tilde{D} < D$ . Table I gives a pseudocode for shrewd selection.



---

**Algorithm 1** Computation of truncated complement using shrewd selection
 

---

**Input:** 2s Hamiltonian  $H_\ell^{2s} = L_{\ell-1}W_\ell W_{\ell+1}R_{\ell+2}$ , 2s wavefunction  $\psi^{2s} = A_\ell \Lambda_\ell B_{\ell+1}$  in bond-canonical form, preselection bond dimension  $D'$ , truncated complement dimension  $\tilde{D}$

**Output:** truncated complement  $\tilde{A}_\ell^{\text{tr}}(\nabla)$

- 1: **function** GETRORTH( $R_{\ell+2}, W_{\ell+1}, B_{\ell+1}, \Lambda_\ell$ )
- 2:   Compute  $R_{\ell+1}^{\text{tmp}} = \Lambda_\ell B_{\ell+1} W_{\ell+1} R_{\ell+2}$
- 3:   Compute  $R_{\ell+1}^{\text{orth}} = R_{\ell+1}^{\text{tmp}} - R_{\ell+1}^{\text{tmp}} B_{\ell+1}^\dagger B_{\ell+1}$
- 4:   **return**  $R_{\ell+1}^{\text{orth}}$
- 5: **end function**
- 6: (Fig. S-2(a)): SVD  $\ell$ -bond of  $R_{\ell+1}^{\text{orth}} = USV^\dagger$
- 7: **function** GETLORTH( $L_{\ell-1}, W_\ell, A_\ell, U, S$ )
- 8:   Compute  $L_\ell^{\text{tmp}} = L_{\ell-1} W_\ell U S$
- 9:   Compute  $L_\ell^{\text{orth}} = L_\ell^{\text{tmp}} - A_\ell A_\ell^\dagger L_\ell^{\text{tmp}}$
- 10:   **return**  $L_\ell^{\text{orth}}$
- 11: **end function**
- 12: (Fig. S-2(b)): SVD  $L_\ell^{\text{orth}} = U' S' V'^\dagger$  and truncate all except the largest  $D'$  singular values in  $S'$ :  $U' S' V'^\dagger \xrightarrow{\text{trunc}} u' s' v'^\dagger$
- 13: (Fig. S-2(c)): Redirect the MPO-leg of  $u' s'$  and perform an SVD on its combined MPO- and  $\ell$ -bond,  $u' s' = \tilde{U} \tilde{S} \tilde{V}^\dagger$ . Truncate all singular values in  $\tilde{S}$  which are numerically zero to ensure  $A_\ell^\dagger \tilde{U} = 0$ . **warning:**  $A_\ell^\dagger \tilde{U} = 0$  is crucial and *must* be ensured!
- 14: (Optional): safety orthogonalization of  $\tilde{U}$  by SVD on  $\tilde{U} - A_\ell A_\ell^\dagger \tilde{U}$  plus truncation of small singular values.
- 15: Assign  $\hat{A}_\ell^{\text{pr}} = \tilde{U}$  ( $\nabla$ )
- 16: **function** GETCORTH( $L_{\ell-1}, W_\ell, W_{\ell+1}, R_{\ell+2}, A_\ell, \Lambda_\ell, B_{\ell+1}, \hat{A}_\ell^{\text{pr}}$ )
- 17:   Compute  $L_\ell^{\text{pr}} = (\hat{A}_\ell^{\text{pr}})^\dagger L_{\ell-1} W_\ell A_\ell$
- 18:   Compute  $C_{\ell+1}^{\text{tmp}} = L_\ell^{\text{pr}} \Lambda_\ell B_{\ell+1} W_{\ell+1} R_{\ell+2}$
- 19:   Compute  $C_{\ell+1}^{\text{orth}} = C_{\ell+1}^{\text{tmp}} - C_{\ell+1}^{\text{tmp}} B_{\ell+1}^\dagger B_{\ell+1}$
- 20:   **return**  $C_{\ell+1}^{\text{orth}}$
- 21: **end function**
- 22: (Fig. S-2(d)): SVD  $C_{\ell+1}^{\text{orth}} = \tilde{U} \tilde{S} \tilde{V}^\dagger$  and truncate all except the largest  $\tilde{D}$  singular values:  $\tilde{U} \tilde{S} \tilde{V}^\dagger \xrightarrow{\text{trunc}} \tilde{u} \tilde{s} \tilde{v}^\dagger$
- 23: Compute  $\tilde{A}_\ell^{\text{tr}} = \tilde{A}_\ell^{\text{pr}} \tilde{u}$  ( $\nabla$ )

---

TABLE I. Pseudocode for computing the truncated complement  $\tilde{A}_\ell^{\text{tr}}$  using shrewd selection.

and singular vectors. We here write bond dimensions with  $*$ , indicating numbers of multiplets (not states), since these determine computational complexities and truncation thresholds and are the quantities shown in the figures. Relations such as  $\tilde{D} = D'w$ , exact for Abelian symmetries where all symmetry multiplets have dimension 1, become approximate,  $\tilde{D}^* \simeq D'^* w^*$ , when written for non-Abelian symmetries.

### B. Options for preselection and final selection

The key idea of CBE is to expand the isometry  $A_\ell(\nabla)$ , whose image (the kept space) initially has dimension  $D_1^*$ , through a direct sum with a so-called truncated comple-

ment, an isometry with image dimension  $\tilde{D}^*$  ( $< D_1^*$ ). The latter is obtained through a suitable truncation of the full complement,  $\bar{A}_\ell(\nabla)$ , whose image (the discarded space) initially has dimension  $\bar{D}^* \simeq D_1^*(d^* - 1)$ . Figure 1 defines three cost functions,  $\mathcal{C}_1$ ,  $\mathcal{C}_2$  and  $\mathcal{C}_3$ , relevant for constructing the truncated complement. The optimal choice for the truncated complement, to be denoted  $\bar{A}_\ell^{\text{tr}}(\nabla)$  here, is obtained by exact minimization of  $\mathcal{C}_1$ , but that requires 2s costs. Therefore, the main text proposes an alternative two-step strategy, requiring only 1s costs. First perform preselection: obtain a preselected complement  $\hat{A}_\ell^{\text{pr}}(\nabla)$ , with image dimension  $\hat{D}^* \simeq D'^* w^*$ , through minimization of  $\mathcal{C}_2$  (Fig. S-2, steps (a-c)). Then perform final selection: obtain the desired truncated complement, denoted  $\tilde{A}_\ell^{\text{tr}}(\nabla)$ , through minimization of  $\mathcal{C}_3$  (Fig. S-2, step (d)).

The minimization of the cost functions  $\mathcal{C}_1$  and  $\mathcal{C}_3$  defined in Fig. 1 involves performing SVDs and truncations of the following two tensors, respectively:

$$\bar{M}^{\text{full}} = \begin{array}{c} \text{Diagram: A tensor with two legs of dimension } \ell \text{ and } \ell+1. \end{array} = \begin{array}{c} \text{Diagram: A tensor with two legs of dimension } \bar{D}^* \text{ and } d^*. \end{array} \simeq \begin{array}{c} \text{Diagram: A tensor with two legs of dimension } \bar{D}^* \text{ and } d^*. \end{array}, \quad (\text{S1a})$$

$$\hat{M}^{\text{pr}} = \begin{array}{c} \text{Diagram: A tensor with two legs of dimension } \ell \text{ and } \ell+1. \end{array} = \begin{array}{c} \text{Diagram: A tensor with two legs of dimension } \hat{D}^* \text{ and } d^*. \end{array} \simeq \begin{array}{c} \text{Diagram: A tensor with two legs of dimension } \hat{D}^* \text{ and } d^*. \end{array}. \quad (\text{S1b})$$

They differ only in one ingredient,  $\bar{A}_\ell^\dagger(\Delta)$  vs.  $\hat{A}_\ell^{\text{pr}\dagger}(\Delta)$ , but since these have vastly different open leg dimensions,  $\bar{D}^*$  vs.  $\hat{D}^*$ , the SVD costs differ vastly too, 2s vs. 1s. The isometries  $\bar{u}$  (yellow) or  $\tilde{u}$  (orange) obtained from the above SVDs and truncations, both with image dimension  $\tilde{D}^*$ , can then be used to construct  $\bar{A}_\ell^{\text{tr}}(\nabla)$  or  $\tilde{A}_\ell^{\text{tr}}(\nabla)$  as follows:

$$\frac{\bar{A}_\ell^{\text{tr}}}{D^* \bar{D}^*} = \frac{\bar{A}_\ell}{\nabla} \bar{u}, \quad (\text{S2a})$$

$$\frac{\tilde{A}_\ell^{\text{tr}}}{D^* \hat{D}^*} = \frac{\hat{A}_\ell^{\text{pr}}}{\nabla} \tilde{u}. \quad (\text{S2b})$$

Both  $\bar{A}_\ell^{\text{tr}}(\nabla)$  and  $\tilde{A}_\ell^{\text{tr}}(\nabla)$  have image dimension  $\tilde{D}^*$ ; the former serves as reference (equivalent to using no preselection,  $D'^* = D^*$ , the latter is an approximation to the former. An even cruder approximation is obtained if one performs preselection without final selection: for that, truncate  $\tilde{U} \simeq \tilde{u}$  in step (c) of Fig. S-2 using  $\hat{D}^* = \tilde{D}^*$  (not  $D'^* w^*$ ), and use the resulting isometry,  $\hat{A}_\ell^{\text{tr}}(\nabla) = \tilde{u}$ , as approximation for  $\bar{A}_\ell^{\text{tr}}(\nabla)$ , omitting step (d) altogether:

$$\frac{\hat{A}_\ell^{\text{tr}}}{D^* \hat{D}^*} = \frac{\tilde{u}}{\nabla}. \quad (\text{S2c})$$

To illustrate the effects of preselection, we will compare four settings: (I) the reference,  $\bar{A}_\ell^{\text{tr}}(\nabla)$ ; or three

versions of preselection with  $D_f^* = D_f^*/w^*$ ,  $0.1D_f^*/w^*$  or 1, to be called (II) *moderate*, (III) *severe* or (IV) *extreme* preselection, respectively, all followed by final selection, yielding three versions of  $\tilde{A}_\ell^{\text{tr}}$  ( $\nabla$ ). Here,  $D_f^*$  is the final bond dimension after an update, obtained by expanding the bond from dimension  $D_i^*$  to  $D_i^* + \tilde{D}^* = D_f^*(1 + \delta)$ , then trimming it back to  $D_f^*$ . To illustrate the importance of final selection we also consider a fifth setting: (V) moderate preselection and  $\hat{U} \simeq \hat{u}$  truncation, without final selection, yielding  $\tilde{A}_\ell^{\text{tr}}$  ( $\nabla$ ).

In the main text, we recommended performing CBE updates using moderate preselection followed by final selection. We showed (Fig. 4(a)) that this yields equally fast convergence per sweep for the GS energy as 2s update. Below, we elucidate why moderate preselection works so well. To this end, we analyze various singular value spectra (Sec. S-1 C) and left singular vectors (Sec. S-1 D), with  $D_f^* = D_{\text{max}}^*$  fixed. We also show that severe and even extreme preselection likewise yield full convergence, albeit at slower rates, by comparing various convergence rates per sweep while increasing  $D_f^*$  (Sec. S-1 E).

### C. Singular values

We start by comparing the singular values of the tensors  $\overline{M}^{\text{full}}$  and  $\overline{M}^{\text{pr}}$ , i.e. the diagonal elements of the diagonal matrices  $\overline{S}$  ( $\blacklozenge$ ) and  $\tilde{S}$  ( $\blacklozenge$ ) in Eqs. (S1), denoted  $\bar{s}_i$  ( $i = 1, \dots, \overline{D}^*$ ) and  $\tilde{s}_i$  ( $i = 1, \dots, \tilde{D}^*$ ), respectively. They differ strongly in number, but if the largest  $\tilde{s}_i$  values roughly mimic the largest  $\bar{s}_i$  values, serving as reference, then preselection is “efficient”, in that it yields essentially optimal results for the dominant singular values.

Figure S-3 compares  $\bar{s}_i$  (grey) and  $\tilde{s}_i$  (orange: moderate or brown: severe preselection) for bond  $\ell = \mathcal{L}/2$  of both the least and most challenging models considered in this work: (a,b) the free fermion chain of Fig. 3, and (c,d) the KHH cylinder of Fig. S-10. Here, we consider the case that  $D_f^*$  has reached  $D_{\text{max}}^*$  and is not grown further, and hence choose  $\tilde{D}^* = D_f^*\delta$  (with  $\delta = 0.1$ ), so that  $D_i^* = D_f^*$ .

For (II) moderate preselection ( $D_f^* = D_f^*/w^*$ ) the  $\tilde{s}_i$  (orange) and  $\bar{s}_i$  (grey) values coincide quite well in the range where they are largest, and eventually drift apart as they get smaller. Especially for the largest  $\tilde{D}^* = D_f^*\delta$  ( $\delta = 0.1$ ) singular values, i.e. the ones that survive final selection and are used for bond expansion, the agreement is rather good (Figs. S-3 (b,d)). This is a very important finding—it indicates that moderate preselection is efficient. By contrast, (III) severe preselection ( $D_f^* = 0.1D_f^*/w^*$ ), shown only in Fig. S-3 (a,b), yields  $\bar{s}_i$  (brown) values that differ substantially from their  $\tilde{s}_i$  (grey) counterparts, even in the range of largest values. Therefore, in this case preselection is too severe to be very efficient.

(We note in passing that when using severe preselection, the corresponding final selection involves almost no further

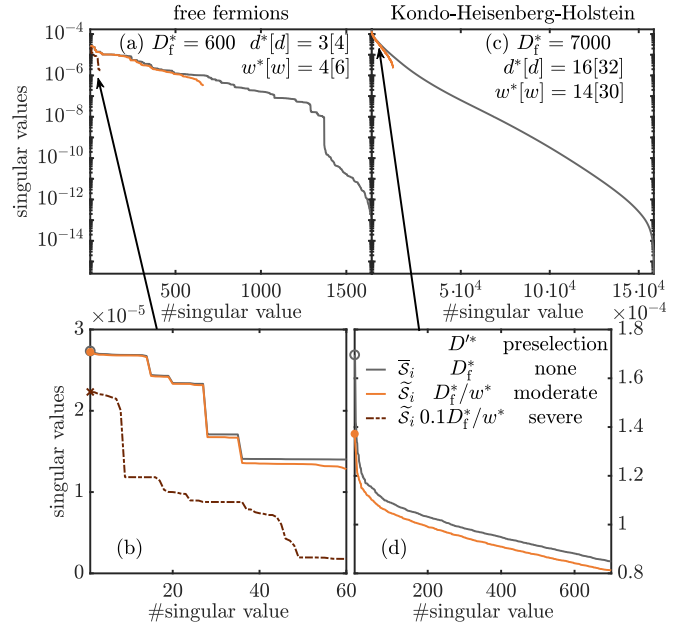


FIG. S-3. Comparison of singular values for three truncation settings (I-III) defined in Sec. S-1 B: the singular values  $\bar{s}_i$  of the tensor  $\overline{M}^{\text{full}}$ , obtained (I) without preselection (reference, grey); and the singular values  $\tilde{s}_i$  of the tensor  $\overline{M}^{\text{pr}}$ , obtained using (II) moderate preselection ( $D_f^* = D_f^*/w^*$ , orange) and (III) severe preselection ( $D_f^* = 0.1D_f^*/w^*$ , brown), all followed by final selection with  $\tilde{D}^* = 0.1D_f^*$ . They are all computed for bond  $\ell = \mathcal{L}/2$  of (a,b) the free fermion chain of Fig. 3, and (c,d) the KHH cylinder of Fig. S-10(d). (b,d) Subsets of the data from (a,c), shown on linear scales, focusing on the range of the largest  $\tilde{D}^* = D_f^*\delta$  singular values  $\bar{s}_i$  and  $\tilde{s}_i$  (with  $\delta = 0.1$ ). This range contains all singular vectors comprising the truncated complement  $\tilde{A}_\ell^{\text{tr}}$  ( $\nabla$ ) obtained after final selection and used for bond expansion. The singular values found with moderate (orange) or no (grey) preselection agree rather well, but those from severe preselection (brown) differ significantly from these.

truncation, since  $\hat{D}^*$  (given by  $\simeq D_f^*w^* = 0.1D_f^*$ ) is almost equal to  $\tilde{D}^*$  (given by  $D_f^*\delta$ ). For the present example, we have  $\hat{D}^* = 63$  and  $\tilde{D}^* = 60$ .)

In Figs. S-3 (a,b), the length of the grey vs. orange lines visually illustrates the main rationale for our CBE strategy: the number of  $\bar{s}_i$  values is generally very much larger than needed for successful bond expansion,  $\overline{D}^* \gg \tilde{D}^*$ . Thus, the 2s full complement subspace (obtained by excluding the 1s variational space from the 2s variational space), is likewise much larger than needed for energy minimization—only a small subspace thereof really matters. CBE aims to identify parts of that small subspace; shrewd selection offers a cheap way of doing so, yielding a notable speedup when computing the truncated complement.

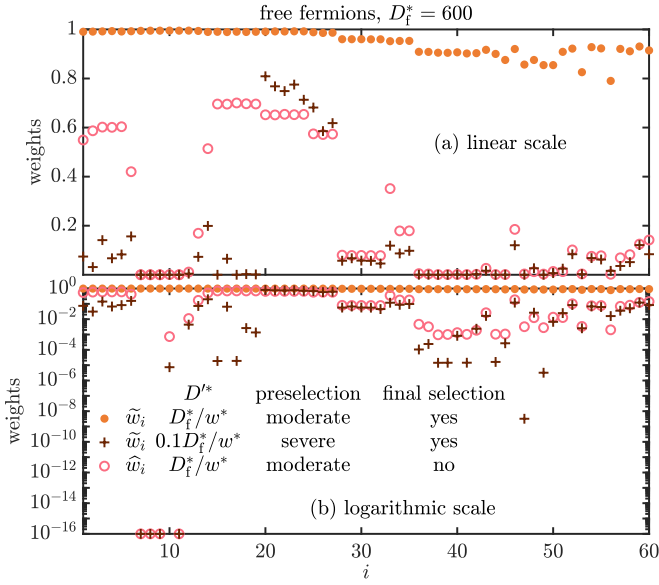


FIG. S-4. Comparison of weights (S3) with which reference singular vectors  $\tilde{s}_i$  from  $\tilde{A}_\ell^{\text{tr}}(\nabla)$  are supported in truncated spaces obtained with three truncation settings (II-IV) defined in Sec. S-1 B:  $\tilde{w}_i$  gives the weight of  $|\tilde{s}_i\rangle$  in  $\text{span}\{|\tilde{s}_j\rangle\}$ , the image of  $\tilde{A}_\ell^{\text{tr}}(\nabla)$ , computed through shrewd selection, using either (II) moderate (orange dots) or (III) severe (brown crosses) preselection; and  $\hat{w}_i$  gives the weight of  $|\tilde{s}_i\rangle$  in  $\text{span}\{|\hat{s}_j\rangle\}$ , the image of  $\hat{A}_\ell^{\text{pr}}(\nabla)$ , computed using (IV) moderate preselection without final selection (pink circles). Both panels show the same data, on (a) a linear and (b) a log scale.

#### D. Singular vectors

We next turn to a comparison of singular vectors to further quantify the benefits of using (II) moderate rather than (III) severe preselection, and of using final selection.

For the latter purpose, we consider a truncation scheme (V) involving moderate preselection but no final selection: after the minimization of the cost function  $\mathcal{C}_2$  (see Fig. S-2(c)), we directly truncate  $\hat{U}\hat{S}\hat{V}^\dagger \simeq \hat{u}\hat{s}\hat{v}^\dagger$  from  $\hat{D}^*$  to  $\hat{D}^*$ , and define the truncated complement as  $\hat{A}_\ell^{\text{tr}} = \hat{u}(\nabla)$ , with singular vectors  $|\hat{s}_i\rangle$ .

To compare singular vectors we compute the weights

$$\tilde{w}_i = \sum_{j=1}^{\tilde{D}^*} |\langle \tilde{s}_j | \tilde{s}_i \rangle|^2 = \begin{array}{c} \text{Diagram showing } \tilde{w}_i \text{ as a sum of squared overlaps} \\ \text{from } \tilde{D}^* \text{ to } i \end{array}, \quad (\text{S3a})$$

$$\hat{w}_i = \sum_{j=1}^{\hat{D}^*} |\langle \hat{s}_j | \tilde{s}_i \rangle|^2 = \begin{array}{c} \text{Diagram showing } \hat{w}_i \text{ as a sum of squared overlaps} \\ \text{from } \hat{D}^* \text{ to } i \end{array}. \quad (\text{S3b})$$

Here,  $\tilde{w}_i$  is the weight with which a singular vector  $|\tilde{s}_i\rangle$  (ordered by size of corresponding singular value) from the image of  $\tilde{A}_\ell^{\text{tr}}(\nabla)$  is supported in the subspace  $\text{span}\{|\tilde{s}_j\rangle\}$ , the image of  $\tilde{A}_\ell^{\text{tr}}(\nabla)$ ; and  $\hat{w}_i$  gives its weight in  $\text{span}\{|\hat{s}_j\rangle\}$ , the image of  $\hat{A}_\ell^{\text{tr}}(\nabla)$ . In less technical

terms, the weights characterize how well reference singular vectors can be represented in these truncated spaces.

These weights are shown in Fig. S-4 for the free fermion data corresponding to Fig. S-3(a). For (II) moderate preselection plus final selection ( $\tilde{w}_i$ , orange dots), all weights are close to one. Thus, this truncation scheme almost perfectly captures that part of the 2s subspace most relevant for minimizing the GS energy. By contrast, for both (III) severe preselection plus final selection ( $\tilde{w}_i$ , brown crosses) and (V) moderate preselection without final selection ( $\hat{w}_i$ , pink circles), most weights are significantly smaller than 1; four are numerically zero. Thus, both these schemes discard a significant part of the space relevant for minimizing the GS energy.

The above analysis illustrates that final selection includes valuable additional information for the  $\hat{D}^* \rightarrow \tilde{D}^*$  truncation, which is not available when truncating  $\hat{S}$  from  $\hat{D}^* \rightarrow \tilde{D}^*$  directly after preselection. This is because the central MPO bond, open during preselection, is *closed* during final selection (compare their cost functions,  $\mathcal{C}_2$  and  $\mathcal{C}_3$  in Fig. 1). Closing the central MPO bond, as appropriate for  $H_\ell^{2s}\psi_\ell^{2s}$ , brings in additional information. The SVD in step (d) of Fig. S-2 involves an additional rotation (encoded in  $\tilde{u}$ ) before the  $\hat{D}^* \rightarrow \tilde{D}^*$  truncation, incorporating this additional information.

#### E. Convergence rate per sweep

The weights obtained for severe preselection ( $D^* = \delta D^*/w^*$ ) in Fig. S-4 pose the question whether  $D^*$  can be too small to give converged results. In this case, preselection would not only be inefficient, but actually unsuccessful. To explore this, Fig. S-5 compares the CBE-DMRG convergence rate for several choices of  $D^*$ , corresponding to (II) moderate (red), (III) severe (green), and (IV) extreme (blue) preselection.

As expected, convergence slows down with smaller  $D^*$ . Remarkably, however, once convergence has been reached, the converged results agree (even for  $D^* = 1$ , a truly extreme choice!). In this sense, the preselection strategy is robust—converged results don’t depend on  $D^*$ . Note, though, that the computation time does not depend significantly on  $D^*$  (provided it is clearly smaller than  $D^*$ ). On the other hand, it obviously does depend on the number of sweeps, and the time per sweep can be very large for expensive models. Therefore,  $D^*$  should not be chosen too small, to avoid a time-costly increase in the number of sweeps.

To summarize: a bond expansion is *efficient*, yielding a significant reduction in GS energy and therefore quick convergence, if  $D^*$  is large enough that the “most important” states  $|\tilde{s}_i\rangle$ , i.e. those with the largest singular values  $\tilde{s}_i$ , are well represented in the expanded space, i.e. have weights  $\tilde{w}_i \simeq 1$ .

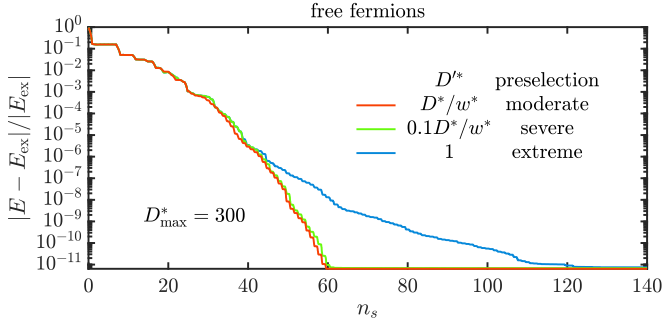


FIG. S-5. Influence of preselection on CBE-DMRG convergence rate, for a half-filled free-fermion chain ( $\mathcal{L} = N = 20$ ). The GS energy is plotted as a function of the number of half-sweeps,  $n_s$ , for three values of  $D^*$ , used for preselection. We start from a  $D_i^* = 1$  valence bond state, set  $\delta = 0.1$ , increase  $D^*$  using  $\alpha = 1.1$  until  $D^* = 300$  is reached, and continue sweeping with  $\alpha = 1$  thereafter.

However, even if  $D^*$  is so small that most of the important states  $|\tilde{s}_i\rangle$  are represented with small weights, a bond expansion can nevertheless be *successful*, in the sense of adding some relevant new states, provided that these weights are non-zero,  $\tilde{w}_i \neq 0$ . The reason is that the states  $|\tilde{s}_i\rangle$  added to  $A_\ell(\nabla)$  contain information about the optimal states  $|\bar{s}_i\rangle$  with finite  $\tilde{w}_i$ , i.e. those  $|\tilde{s}_i\rangle$  are not orthogonal to the expanded kept space. As long as this information is available, subsequent 1s updates will optimize the kept sector accordingly; the states  $|\tilde{s}_i\rangle$  just offer a somewhat less optimal starting point for that than the  $|\bar{s}_i\rangle$ .

Note that it is of utmost importance for successful bond expansion that information on the *most important*  $|\bar{s}_i\rangle$  is included. Since only a small set of states is in the end used for expansion, the most important states must be prioritized; otherwise, inferior information is included in the kept space, rendering the bond expansion unsuccessful: Subsequent 1s updates may then optimize towards a suboptimal kept sector, as the optimal one may not be available to the 1s update, e.g. due to symmetry constraints. The energy will still decrease due to the unsuccessful bond expansion plus 1s update, but not as much as if the correct information on the most important  $|\bar{s}_i\rangle$  is correctly included. The result will be a suboptimal final state at the desired finite bond dimension  $D_{\max}^*$ , i.e. we have wasted resources.

Fig. S-5 shows that CBE-DMRG correctly includes information on the most optimal states when expanding the bond, independent of  $D^*$ . Even with extreme preselection ( $D^* = 1$ ), it does not get stuck with some sub-optimal state at  $D_{\max}^* = 300$ , but eventually converges (albeit slowly) to the same GS as found with larger choices of  $D_{\max}^*$ .

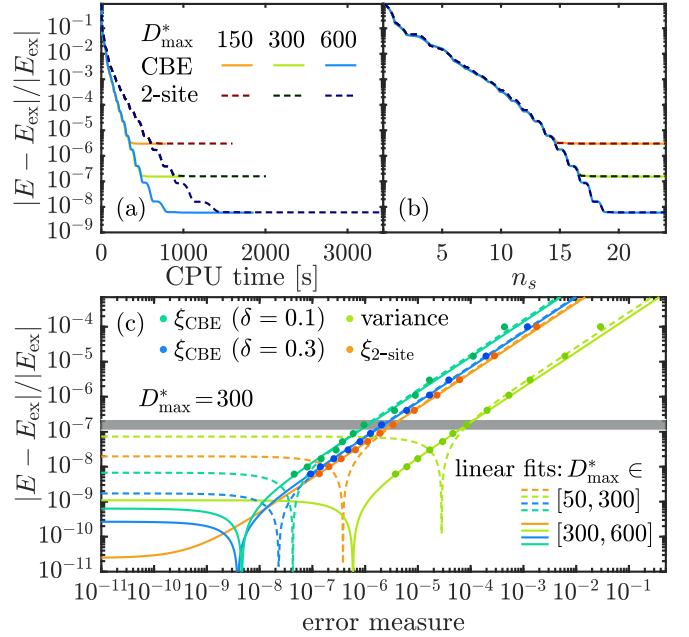


FIG. S-6. Benchmark results for free fermions. Relative error in GS energy vs. (a) CPU time  $xt$  and (b) number of half-sweeps  $n_s$ , for CBE and 2s DMRG.  $E_{\text{ex}}$  is the exact GS energy. (c) Quality of linear extrapolation of the GS energy using various error measures. Dashed (solid) lines show linear fits to data points lying on or above (on or below) the grey bar, computed using  $D_{\max}^* \leq 300$  ( $\geq 300$ ), representing intermediate (high) accuracy calculations; when these lines touch zero, the extrapolated error changes sign.

## S-2. SIMPLE BENCHMARK: FREE FERMIONS

In this section, we benchmark CBE-DMRG for free fermions in one dimension (1D). The main purpose is to evaluate the validity of the CBE discarded weight as an error measure usable for extrapolation on an exactly solvable model and compare it to other established error measures. All CPU time measurements were done on a single core of an Intel Core i7-9750H processor.

Consider a chain of spinful free fermions, exactly solvable but non-trivial for DMRG, with Hamiltonian  $H_{\text{FF}} = -\sum_{i=1}^{\mathcal{L}-1} \sum_{\sigma} (c_{i\sigma}^\dagger c_{i+1\sigma} + \text{h.c.})$  and  $\mathcal{L} = 100$  sites. We exploit  $U(1)_{\text{ch}} \otimes \text{SU}(2)_{\text{sp}}$  charge and spin symmetry, with local dimension  $d^* [d] = 3[4]$ . The MPO dimension is  $w^* [w] = 4[6]$ . We seek the GS in the sector with total spin  $S=0$ , at half-filling, with particle number  $N = \mathcal{L}$ .

Figure S-6(a) plots the relative error in energy vs. CPU time for different  $D_{\max}^*$  for both CBE and 2s schemes; Fig. S-6(b) plots it vs. the number of half-sweeps  $n_s$ . While convergence with  $n_s$  is comparable for CBE and 2s, CBE requires less CPU time than 2s by a factor of  $\simeq 2$ . (This speedup factor is less than  $d^* = 3$ , since  $d^*$  is quite small and steps not involving the iterative eigensolver have the same numerical cost for both CBE and 2s schemes.)

Figure S-6(c) shows linear-fit extrapolations of the energy in terms of the discarded weight  $\xi$  and the 2s variance



(the latter computed following Ref. [28]). The quality of the extrapolations is comparable for all considered methods: they all reduce the error in energy by roughly one order compared to the most accurate data point considered, as expected [25, 28]. The error is smaller for  $\delta = 0.3$  than for  $\delta = 0.1$ , and its dependence on discarded weight is slightly less noisy (though this hardly affects the extrapolation).

### S-3. COMPARISON OF CBE TO DMRG3S

In this section, we provide a comparison between DMRG3S and CBE-DMRG. First, we formulate DMRG3S in terms of the kept-discarded ( $\kappa$ D) space language developed by us in Ref. 27 and also used in this paper. Based on that, we then discuss to what extent the bond-expansion term in DMRG3S is different to that occurring in CBE-DMRG. We then compare the performance of DMRG3S and CBE-DMRG based on two models.

#### A. DMRG3S in $\kappa$ D language

In case of a right-to-left sweep, DMRG3S expands and truncates the right isometry as follows:

$$H_\ell^{1s,3S} \stackrel{(d)}{=} \left[ \text{diamond} \right] = \left[ \text{diamond} \right]^D, \quad (S4)$$

where  $\blacklozenge$  represents a unitary, in analogy to Eq. (6) in the main text. Here,  $C_{\ell+1}$  is direct-summed with the expansion term multiplied by a mixing parameter  $\alpha$ , then (a) singular value decomposed and (b) truncated to bond dimension  $D$ , yielding the new isometry  $B_{\ell+1}^{3S}$ . Finally in steps (c) and (d),  $C_\ell$  and  $H_\ell^{1s}$  are “expanded”, respectively, similar to CBE (DMRG3S first updates  $C_{\ell+1}$  and then uses the mixing expansion of Eq. (S4) to expand  $B_{\ell+1}$ ; by contrast, CBE first expands  $A_\ell$  via Eq. (9), then updates  $C_{\ell+1}$ ). Note that in step (c),  $C_\ell^{3S,i}$  needs to be normalized explicitly because

$$\text{diamond} \neq \text{diamond}^{3S}, \quad (S5)$$

i.e. the kept space spanned by the old isometry  $B_{\ell+1}$  is not fully contained in the new one,  $B_{\ell+1}^{3S}$ , since part of the kept space has been truncated. Finally,  $C_\ell^{3S}$  is

updated with the GS of  $H_\ell^{1s,3S}$  obtained with an iterative eigensolver (Lanczos in our case), initialized with  $C_\ell^{3S,i}$ .

Our CBE strategy differs from DMRG3S in the following ways:

- (i) When constructing the expansion term, CBE considers  $H_\ell^{2s}\psi_\ell^{2s}$ , i.e. the action of the full 2s Hamiltonian on the 2s wavefunction. By contrast, DMRG3S only considers part of  $H_\ell^{2s}\psi_\ell^{2s}$  (the right “half” in the right-to-left sweep discussed here). We found however that considering  $H_\ell^{2s}\psi_\ell^{2s}$  fully is crucial to not experience convergence issues. Note that the expansion term in DMRG3S is more heuristic than that in CBE and does not have the interpretation of an effective Hamiltonian acting on a wavefunction.
- (ii) CBE projects  $H_\ell^{2s}\psi_\ell^{2s}$  fully to the DD sector, i.e. the image of the orthogonal complements  $\bar{A}_\ell \otimes \bar{B}_{\ell+1}$  ( $\nabla \otimes \nabla$ ). This ensures that the kept space is not truncated during the bond expansion and crucially, the energy of the variational wavefunction remains the same. By contrast, DMRG3S does not involve any DD or D projections. Thus, part of the  $\kappa$  sector is usually truncated during the DMRG3S bond expansion, raising the energy of the variational wavefunction. Thus, CBE-DMRG is fully variational (bond expansion does not lead to a less optimal wavefunction) while DMRG3S is not (see also the discussion of Fig. 1 of Ref. 26).

(iii) Because DMRG3S changes the variational wavefunction by truncating part of the  $\kappa$  sector, the weight of the expansion term in DMRG3S has to be controlled by a heuristic mixing factor  $\alpha$  to ensure the variational energy is not raised too much. This mixing factor has to be carefully adapted during the calculation to ensure reliable convergence and is model dependent (see Ref. 26 Sec. VI). By contrast, there is no such mixing parameter in CBE. In CBE, there is a parameter  $\delta$  which controls the amount of bond expansion. We found however that CBE-DMRG is not at all sensitive to the value of  $\delta$  and most important,  $\delta$  is not model dependent. Indeed, we have set  $\delta = 0.1$  in our CBE calculations independent of the model. Further,  $\delta$  remains constant during the calculation.

Note that if 3S would include projections to the D sector and would not truncate part of the kept space during expansion, it would be similar to CBE without preselection and final selection. However, leaving out preselection is expensive while leaving out final selection is inefficient (see Sec. S-1).

#### B. Results

We now benchmark the accuracy and speed of DMRG3S against that of CBE-DMRG. For that, we use three models: a 1D Hubbard-Holstein model, spinful free fermions on a short 4-leg cylinder and a free fermion chain with only next-nearest neighbor hopping. All CPU time measurements were done on a single core of an Intel Core

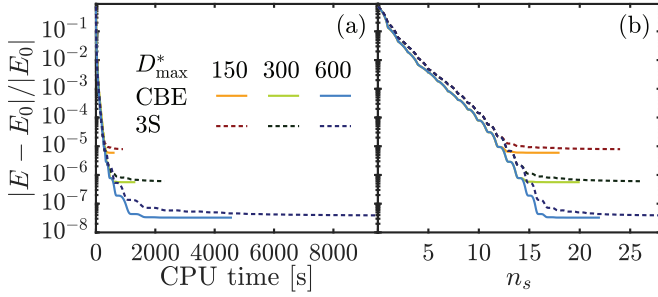


FIG. S-7. Error in energy for the Hubbard-Holstein (HH) model versus (a) CPU time and (b) number of half-sweeps  $n_s$ , computed using CBE-DMRG (solid) or DMRG3S (dashed).  $E_0$  is obtained via  $\xi$ -extrapolation of calculations done at  $D^* \geq 1000$ .

i7-9750H processor.

*Hubbard-Holstein model.*— We start our comparison with the 1D Hubbard-Holstein model [32–36], with Hamiltonian

$$H_{\text{HH}} = - \sum_{i\sigma} (c_{i\sigma}^\dagger c_{i+1\sigma} + \text{h.c.}) + U \sum_i n_{i\uparrow} n_{i\downarrow} \quad (\text{S6})$$

$$+ \omega_{\text{ph}} \sum_i b_i^\dagger b_i + g \sum_i (n_{i\uparrow} + n_{i\downarrow} - 1) (b_i^\dagger + b_i).$$

We chose  $U = 0.8$ ,  $g = \sqrt{0.2}$ ,  $\omega_{\text{ph}} = 0.5$ ,  $\mathcal{L} = N = 100$ , total spin  $S=0$ , and restrict the maximum local number of excited phonons to  $N_{\text{ph}}^{\text{max}} = 3$ . Both CBE-DMRG and DMRG3S are initialized with the same  $D^* = 1$  MPS with uniform charge distribution and the bond dimension is grown by a factor of  $\sqrt{2}$  every half sweep, i.e. it is doubled every sweep. The DMRG3S mixing parameter is adapted according to the prescription described in Ref. 26, Sec. VI.

Figures S-7 (a) and (b) show a comparison between the error in energy versus CPU time and number of sweeps, respectively, for different bond dimensions. As a function of CPU time, the error in energy of DMRG3S initially converges at the same rate as CBE-DMRG. Subsequently, however, the convergence of 3S slows down compared to CBE, ultimately requiring significantly more CPU time to reach the final converged result. Further, the final converged 3S result is not as accurate as the CBE result, though this is more severe at small  $D^*$  than at large  $D^*$ . At  $D^* = 150$ , the relative error from 3S is about 1.3 times that of CBE.

*Spinful free fermion cylinder.*— For our next benchmark, we use free fermions on a  $\mathcal{L}_x \times \mathcal{L}_y = 10 \times 4$  cylinder, described by  $H_{\text{cyl}} = - \sum_{\langle \ell, \ell' \rangle, \sigma} (c_{\ell\sigma}^\dagger c_{\ell'\sigma} + \text{h.c.})$ . We search for the GS with  $N = \mathcal{L}_x \cdot \mathcal{L}_y$  and  $S = 0$ . Again, we start with a  $D^* = 1$  state with uniform charge distribution and increase the bond dimension by a factor of  $\sqrt{2}$  every half-sweep.

Figures S-8 (a) and (b) show a comparison of the error in energy versus CPU time and the number of sweeps obtained with both CBE and 3S, respectively. Again,

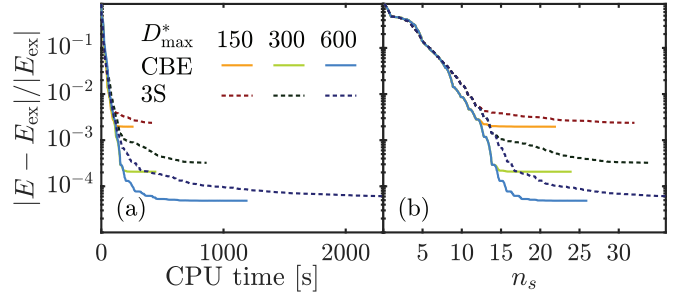


FIG. S-8. Error in energy for spinful free fermions on a  $10 \times 4$  cylinder versus (a) CPU time and (b) number of half-sweeps  $n_s$ .  $E_{\text{ex}}$  is the exact ground-state energy.

CBE and 3S initially converge at the same rate w.r.t. CPU time, but DMRG3S eventually slows down and takes longer to reach final convergence compared to CBE. Further, for all considered bond dimensions, 3S converges now to a noticeably larger error, about 1.2 to  $>1.5$  times that of CBE.

*Next-nearest neighbor free fermion chain.*— As a last model for our comparison, we choose free fermions on a chain with only next-nearest neighbor hopping, described by  $H_{\text{nnn}} = - \sum_{\ell=1}^{\mathcal{L}-2} (c_\ell^\dagger c_{\ell+2} + \text{h.c.})$ . Choosing  $\mathcal{L} = 100$  and exploiting  $U(1)_{\text{ch}}$  symmetry, we initialize DMRG with a half-filled product state consisting of a succession of two occupied sites followed by two empty sites.

As shown in Fig. S-9(a), this rather simple model initialized with the product state described above poses a serious challenge to 2s DMRG, which does not converge. The reason for the failure of 2s DMRG is that the initial state has  $\Delta_{E^\perp}^1 = 0$  and  $\Delta_{E^\perp}^2 = 0$  (c.f. Eq. (8)), implying that  $H_\ell^{2s} \psi_\ell^{2s}$  is parallel to  $\psi_\ell^{2s}$ . From the perspective of 2s DMRG, the initial state is therefore an eigenstate.

By contrast, both DMRG3S and CBE-DMRG do converge, with CBE-DMRG again reaching convergence faster in terms of number of sweeps and converging to a slightly lower energy than DMRG3S. During the initial few sweeps, CBE-DMRG lowers the energy somewhat

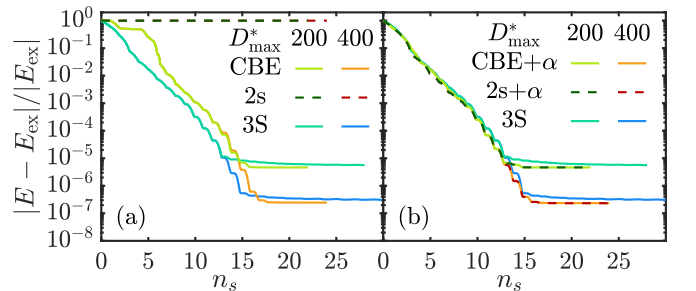


FIG. S-9. Error in energy for the next-nearest neighbor free fermion chain, computed using CBE and 2s, (a) without mixing, and (b) with mixing ( $\alpha = 0.1$ ), during the initial 14 half-sweeps. DMRG3S results in (a) and (b) are the same data.  $E_{\text{ex}}$  is the exact ground-state energy.

more slowly than DMRG3S, reflecting the close relation between CBE–DMRG and 2s DMRG. In contrast to the latter, however, CBE–DMRG eventually does converge. The reason is that CBE expands the MPS bond from  $D$  to  $D + \tilde{D}$  even if the projection of  $H_\ell^{2s}\psi_\ell^{2s}$  to DD yields zero — indeed, final selection (Fig. 2(d)) generates  $\tilde{D}$  additional states even if some or all of the associated singular values (from  $\tilde{s}$  in Fig. 2(d)) are numerically zero. This enlarges the kept space from  $D$  to  $D + \tilde{D}$ , such that eventually  $\Delta_E^{1\perp}$  becomes nonzero and the energy can be lowered during the CBE 1s update.

As suggested in Ref. 7, Section 3.1, adding noise terms in the spirit of DMRG3S or density matrix perturbation of Ref. 25 during the initial few sweeps can help 2s DMRG to converge. The same is true for CBE–DMRG, which also struggles during the initial sweeps in the present case, as mentioned above. To demonstrate this, we therefore performed 2s and CBE calculations combined with DMRG3S mixing, dubbed 2s+ $\alpha$  and CBE+ $\alpha$ , respectively. (For CBE+ $\alpha$ , first the CBE expansion of  $A_\ell$  according to Eq. (9) is used, then  $C_{\ell+1}$  is updated, and finally a mixing expansion of  $B_{\ell+1}$  according to Eq. (S4) is used.) We choose  $\alpha = 0.1$  during the initial 7 sweeps (i.e. 14 half-sweeps) and then continue without mixing. Note that we do not need to fine-tune  $\alpha$ , in contrast to DMRG3S. The results of this strategy are displayed in Fig. S-9(b), which shows that both 2s+ $\alpha$  and CBE+ $\alpha$  converge similarly w.r.t. the number of sweeps.

*Summary of CBE to DMRG3S comparison.*— CBE generically converges significantly faster w.r.t. number of sweeps than 3S but takes about the same CPU time per sweep. This leads to overall significantly faster convergence of CBE compared to 3S. Further, the accuracy of CBE is generically better than that of 3S at the same bond dimension, meaning that CBE uses variational resources more efficiently than 3S. This seems to be especially the case for more challenging models where single-site methods provide the most benefit due to reduced computational demands. An exception are situations where 2s DMRG fails entirely. In such cases, the convergence during the initial few sweeps is significantly slower for CBE than DMRG3S (though CBE eventually catches up, ultimately reaching a lower final energy than DMRG3S). The initial CBE convergence can be sped up, if desired, by including some mixing during the first few sweeps, using a mixing parameter that need not be fine-tuned. This strategy is the one we would recommend as standard practice when dealing with challenging models.

#### S-4. KONDO-HEISENBERG CYLINDERS

In this section, we provide supplementary information on the two most challenging models considered in this work, both defined on a 4-leg cylinder: the Kondo-Heisenberg (KH) model discussed in the main text, where

we presented evidence for Fermi surface (FS) reconstruction; and the Kondo-Heisenberg-Holstein (KHH) model, included here to demonstrate the feasibility of using CBE for tackling truly complex models.

The KH model is relevant for heavy-fermion materials, which consist of itinerant conduction electrons, hybridizing with localized  $f$  orbitals [37]. At low energies, only the spin degree of freedom of the  $f$  electrons remain, describable by a KH model,

$$H_{\text{KH}} = - \sum_{\sigma=\uparrow,\downarrow} \sum_{\langle \ell, \ell' \rangle} (c_{\ell\sigma}^\dagger c_{\ell'\sigma} + h.c.) \quad (\text{S7})$$

$$+ J_K \sum_{\ell} \mathbf{S}_\ell \cdot \mathbf{s}_\ell + J_H \sum_{\langle \ell, \ell' \rangle} \mathbf{S}_\ell \cdot \mathbf{S}_{\ell'}.$$

Here,  $c_{\ell\sigma}^\dagger$  is a fermionic creation operator at site  $\ell = (x, y)$  with spin  $\sigma$ ,  $\mathbf{s}_\ell = \frac{1}{2} \sum_{ss'} c_{\ell s}^\dagger \boldsymbol{\sigma}_{ss'} c_{\ell s'}$  is the corresponding electron spin operator and  $\mathbf{S}_\ell$  the spin operator of a spin- $\frac{1}{2}$  local moment, all for site  $\ell$ .

The KHH model is obtained from the KH model by additionally including Holstein phonons, motivated by experimental data suggesting that phonons may play a role in heavy-fermion physics [38]:

$$H_{\text{KHH}} = H_{\text{KH}} + \omega_{\text{ph}} \sum_{\ell} b_\ell^\dagger b_\ell + g \sum_{\ell\sigma} (n_{\ell\sigma} - \frac{1}{2}) (b_\ell^\dagger + b_\ell). \quad (\text{S8})$$

Here,  $b_\ell^\dagger$  is phonon creation operator for site  $\ell$ . To deal with the infinite local phonon Hilbert space, we restrict the maximum number of local phonon excitations to  $N_{\text{ph}}^{\text{max}}$  (specified below) in our DMRG calculations.

In Sec. S-4A we first show stable convergence of CBE–DMRG for the KHH model on a  $10 \times 4$  cylinder. Then, in Sec. S-4B, we describe how to extract information on the FS in  $40 \times 4$  KH cylinders from ground states computed with CBE–DMRG. Finally, in Sec. S-4C, we show that our KH cylinder results are consistent with Luttinger’s sum rule, relating the electron density to the FS volume.

##### A. Kondo-Heisenberg-Holstein cylinders: convergence

Our intention is to show that CBE–DMRG is stable for the KHH model, which is at the edge of what is possible with current DMRG techniques. To check the applicability of CBE–DMRG to the KHH model on a  $10 \times 4$  cylinder, we use Kondo coupling  $J_K = 5$ , Holstein coupling  $g = 0.5$  to the phonons and optical phonon frequency  $\omega_{\text{ph}} = 0.5$ . We considered two different values for  $N_{\text{ph}}^{\text{max}} \in \{0, 3\}$  and the Heisenberg coupling  $J_H \in \{0, 0.5\}$ .

We performed GS searches for  $N = \mathcal{L}(1 + \frac{1}{4}) = 50$  and  $S = 0$ , i.e. at 25% electron doping. Figure S-10 shows the energy error vs.  $\xi$  for four parameter combinations

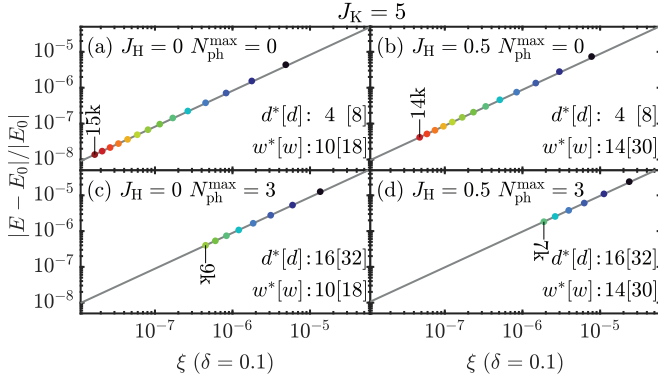


FIG. S-10. Error in GS energy versus discarded weight for the Kondo-Heisenberg-Holstein (KHH) model on a  $10 \times 4$  cylinder, with (a) only Kondo coupling, (b) Kondo and Heisenberg coupling, (c) Kondo and Holstein coupling and (c) Kondo, Heisenberg and Holstein coupling. Legends state our choices for  $J_H$  and  $N_{\text{ph}}^{\text{max}}$ , and corresponding values of  $d^*[d]$  and  $w^*[w]$ . For each panel,  $E_0$  was obtained by linear  $\xi$ -extrapolation to  $\xi=0$  (grey line) using the four largest  $D^*$  values. The very largest  $D^*$  is shown next to its data point;  $D^*$  changes by 1k between adjacent data points.

(see legends). The linear  $\xi$ -dependence of  $E$  demonstrates proper convergence of CBE-DMRG. Very large  $D^*$  values are achievable despite the rather huge values of  $d$  and  $w$ . This is remarkable especially for  $J_H=0.5$  and  $N_{\text{ph}}^{\text{max}}=3$  (Fig. S-10(d)), where  $d^*[d]=16[32]$  and  $w^*[w]=14[30]$  are large, so that 2s schemes become excessively costly. These results encouragingly illustrate the potential of CBE for handling very complex models.

## B. Kondo-Heisenberg cylinders: Fermi surface

Having established stable convergence of CBE-DMRG for the KHH model on a  $10 \times 4$  cylinder, we turn to the Kondo-Heisenberg (KH) model on longer  $40 \times 4$  cylinders. In this section, we provide some supplementary information on our discussion of the Fermi surface (FS) reconstruction in the KH model.

Heavy-fermion materials feature many interesting phenomena. One that is not so well understood is the so-called Kondo breakdown (KB) quantum critical point (QCP). When the system is tuned across this KB-QCP, the FS volume abruptly changes [39], leading to a violation of Luttinger's sum rule [40] and strange metal behavior at finite temperatures.

In Fig. 6 of the main text, we have shown strong evidence for the existence of two distinct phases with different FS volumes in the KH model on a 4-leg cylinder. This in turn strongly suggests the existence of a KB-QCP in the KH model on 4-leg cylinders, which can be studied in a non-perturbative, controlled and unbiased way using our newly developed CBE-DMRG method. Here, our goal is to explain in detail how we extracted the Fermi points from our CBE-DMRG data on the  $40 \times 4$  KH cylinder,

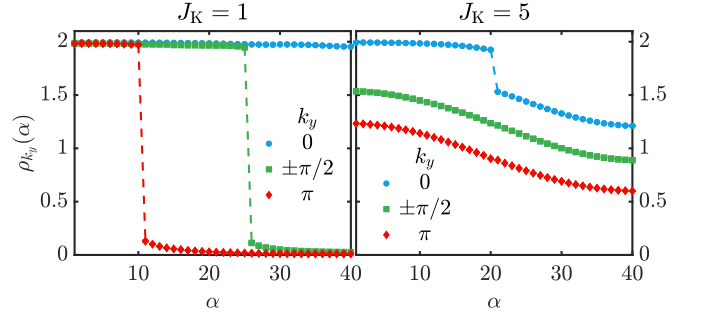


FIG. S-11.  $k_y$ -resolved eigenvalues,  $\rho_{k_y}(\alpha)$  of the single-particle density matrix of the Kondo-Heisenberg (KH) model on a  $40 \times 4$  cylinder at 25% electron doping,  $J_H = 0.5$  and (a)  $J_K = 0.5$  and (b)  $J_K = 2.5$ . Eigenvalues are extrapolated to truncation error  $\xi \rightarrow 0$ , error bars are below symbol sizes. Dashed lines highlight jumps in the spectra.

thereby establishing the two distinct phases reported in the main text. We leave the study and discussion of a possible KB-QCP and its rich physics to future work.

To illustrate our Fermi point extraction strategy, we here focus on  $J_K = 1$  and  $J_K = 5$ , representative for the two phases with different Fermi surfaces at small and large  $J_K$ , respectively. We extract the Fermi points from the single-particle density matrix,

$$\rho_{k_y}(x, x') = \sum_{\sigma} \langle c_{x k_y \sigma}^{\dagger} c_{x' k_y \sigma} \rangle, \quad (\text{S9})$$

where  $c_{x k_y \sigma} = \frac{1}{2} \sum_{y=1}^4 e^{i k_y y} c_{x y \sigma}$ , with  $k_y \in \{0, \pm \frac{\pi}{2}, \pi\}$ , is the  $y$ -Fourier transform of the fermionic annihilation operator  $c_{x y \sigma} = c_{\ell \sigma}$ .

Figure S-11 shows the eigenvalues of  $\rho_{k_y}(x, x')$ , dubbed  $\rho_{k_y}(\alpha)$ , for given  $k_y$  (extrapolated to zero discarded weight  $\xi$ ). The structure of the eigenvalue spectra for  $J_K = 1$  and  $J_K = 5$  differ qualitatively: For  $J_K = 1$ , they show a jump for  $k_y = \pm \frac{\pi}{2}$  and  $k_y = \pi$ , but not for  $k_y = 0$ , while for  $J_K = 5$  it is the other way around.

A jump in  $\rho_{k_y}(\alpha)$  suggests that the corresponding  $k_y$  value is visited by the Fermi surface, i.e. there exists a point on the FS with Fermi wavevector  $\mathbf{k}_F = (k_{F_x}(k_y), k_y)$ . Note, however, that since we use open boundary conditions, the eigenbasis of  $\rho_{k_y}$  is not the Fourier basis. We

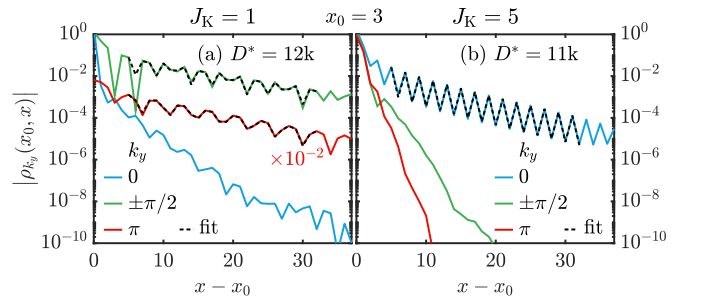


FIG. S-12. Absolute values of the off-diagonal elements of the single-particle density matrix of the Kondo-Heisenberg model on a  $40 \times 4$  cylinder at 25% electron doping, for  $J_H = 0.5$  and (a)  $J_K = 1$ , (b)  $J_K = 5$ . Solid lines are CBE-DMRG data; black dotted lines are fits to Eq. (S10) to extract  $\lambda$  and  $k_{F_x}$ .



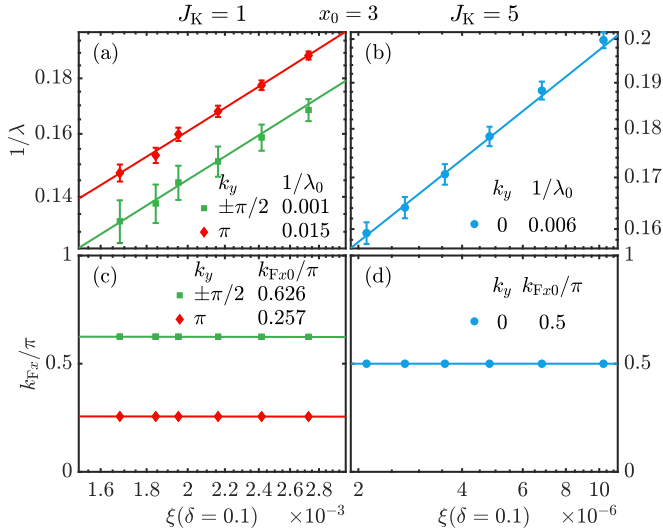


FIG. S-13. Discarded weight extrapolation of (a,b) the correlation length and (c,d) the corresponding Fermi wavevectors, obtained through the fits of  $\rho_{k_y}(x_0, x)$  to Eq. (S10), as shown in Fig. S-12. Error bars indicate 68.2% confidence intervals (i.e. one standard deviation) for the fit parameters (below symbol size in (c,d)).

can therefore not rely on the eigenbasis of  $\rho_{k_y}$  to determine the corresponding  $x$ -direction Fermi wavevector  $k_{F_x}(k_y)$ . Instead, we use the off-diagonal elements  $\rho_{x_0 x}(k_y)$  in the real space basis, for fixed  $x_0 = 3$ , and study the behaviour of  $\rho_{k_y}(x_0, x)$  as a function of  $|x - x_0|$ . The expected behaviour in the case of a Fermi point can be parametrized by the Ansatz

$$\rho_{k_y}(x_0, x) \sim \cos(k_{F_x}(k_y)|x - x_0| + \phi) \frac{e^{-|x - x_0|/\lambda}}{|x - x_0|^\alpha}. \quad (\text{S10})$$

Here, the exponent in the denominator is given by  $\alpha = 1$  in case of a Fermi liquid (obtained by Fourier transforming a step function), or takes some non-universal, interaction-dependent value in the case of a Luttinger liquid [41]. Because CBE-DMRG approximates the true ground state by a MPS, the correlation length  $\lambda$  is finite. When  $D^* \rightarrow \infty$ , or equivalently when  $\xi \rightarrow 0$ , we expect  $\lambda \rightarrow \infty$ . In Fig. S-12, we show that a fit of  $\rho_{k_y}(x_0, x)$  to Eq. (S10) indeed works well for those  $\rho_{k_y}$  with gapped spectrum (green, red curves in Fig. S-11(a), blue curve in Fig. S-11(b)). Note that such fits are not possible for the remaining cases.

Figures S-13(a,b) show the behaviour of the inverse correlation length  $1/\lambda$  versus discarded weight  $\xi$ . In the cases where we have identified a possible Fermi wavevector  $k_{F_x}(k_y)$ ,  $1/\lambda$  indeed extrapolates to zero (i.e.  $\lambda \rightarrow \infty$ ) within our numerical accuracy, consistent with expectations for either a Fermi or Luttinger liquid. In Fig. S-13(c,d), we show the corresponding Fermi wavevectors  $k_{F_x}(k_y)$  plotted against discarded weight  $\xi$ . It turns out that  $k_{F_x}(k_y)$  is almost independent of  $\xi$ , which means the determination of  $k_{F_x}(k_y)$  is highly accurate.

Our way of extracting Fermi wavevectors from DMRG ground states using the single-particle density matrix is reliable and numerically robust. In Fig. 5 of the main text, we only presented Fermi wavevectors for values of  $J_K$  where we were able to converge the DMRG calculation with reasonable numerical effort ( $D^* \leq 12k$  on the  $40 \times 4$  cylinder). Closer to the putative KB-QCP, more numerical resources are needed. These more challenging calculations are beyond the scope of the current work (which mainly focuses on the development of the CBE method) and are left for the future.

### C. Kondo-Heisenberg cylinders: Fermi volume and Luttinger's sum rule

The FS is especially interesting in the context of Luttinger's sum rule [40, 42],

$$n_{\text{eff}} = 2v_{\text{FS}} \quad (\text{S11})$$

(prefactor 2 for spin). It links the volume enclosed by the FS,  $v_{\text{FS}}$  (measured in terms of Brillouin zone volumes), to the effective number of mobile charge carriers  $n_{\text{eff}}$  (defined modulo 2, i.e. excluding filled bands).

An unambiguous definition of the volume of the FS must include a criterion distinguishing its inside and outside. The inside of the Fermi volume is usually defined as those momentum space states which are "filled", having  $n_{\mathbf{k}} = \sum_{\sigma} \langle c_{\mathbf{k}\sigma}^\dagger c_{\mathbf{k}\sigma} \rangle \simeq 2$ . We point out that the criterion based on  $n_{\mathbf{k}} \in \{0, 2\}$  can only take two values, which is not the case for interacting systems. A stringent criterion for interacting systems can be formulated in terms of single-electron Green's functions (see, e.g., Ref. 44, Eq. (7)), but the computation of such dynamical quantities is beyond the scope of this work. Here, we take the heuristic approach based on  $n_{\mathbf{k}}$ .

To make progress on a formula for  $v_{\text{FS}}$  in 2D, we assume that single-electron states in the vicinity of  $\mathbf{k} = (0, 0)$  are usually lower in energy than those in the vicinity of  $\mathbf{k} = (\pi, \pi)$ . Thus, we consider the states between  $\in [-k_{F_x}(k_y), k_{F_x}(k_y)]$  filled. For an infinite 2D system, we can now compute

$$v_{\text{FS}} = \int_{-\pi}^{\pi} \frac{dk_y}{2\pi} \int_{-k_{F_x}(k_y)}^{k_{F_x}(k_y)} \frac{dk_x}{2\pi} = \int_{-\pi}^{\pi} \frac{dk_y}{2\pi} \frac{|k_{F_x}(k_y)|}{\pi}. \quad (\text{S12})$$

Our KH cylinders at hand are however not infinite 2D systems due to the finite circumference of  $\mathcal{L}_y = 4$  (the finite length  $\mathcal{L}_x$  can in practice be chosen large enough to not play a conceptually problematic role). In this case, we replace the integral in Eq. (S12) by a sum to obtain

$$v_{\text{FS}} = \frac{1}{\mathcal{L}_y} \sum_{k_y} |k_{F_x}(k_y)|/\pi. \quad (\text{S13})$$

Note that we are now faced with the ambiguity of how to define  $k_{Fx}(k_y)$  for those  $k_y$  values for which no Fermi points exist. The corresponding  $k_{Fx}(k_y)$  could be either  $\pi$  or 0, depending on whether  $n_{\mathbf{k}}$  is filled or empty for all  $k_x$ , respectively. For  $\mathcal{L}_y \rightarrow \infty$ , this can be decided based on continuity of  $k_{Fx}(k_y)$ . By contrast, for finite  $\mathcal{L}_y$ , where  $k_y$  takes only discrete values, the definition of  $k_{Fx}(k_y)$  has to be based on heuristic arguments. To this end, we use the eigenvalues of the single-particle density matrix  $\rho_{k_y}(\alpha)$  (see Fig. S-11) as a proxy for  $n_{\mathbf{k}}$  (in the limit  $\mathcal{L}_x \rightarrow \infty$ , these quantities coincide). If the eigenvalues  $\rho_{k_y}(\alpha)$  are close to (or not close to) 2 for *all*  $\alpha$ , we take that as an indication that all states are filled (or empty), and accordingly define  $k_{Fx}(k_y) = \pi$  (or = 0).

For  $J_K = 1$ , only  $k_{Fx}(k_y = 0)$  is undecided. Since  $\rho_0(\alpha) \simeq 2$  (see Fig. S-11(a), blue dots), we define  $k_{Fx}(0) = \pi$ . Together with the Fermi points found at  $k_y = \pm \frac{\pi}{2}, \pi$ , we thus find  $(|k_{Fx}|, |k_y|) = (\pi, 0), (0.625\pi, \frac{\pi}{2})$  and  $(0.256\pi, \pi)$ , matching the free-electron values at  $J_K =$

0. Inserting these into Eq. (S13), we find  $v_{FS} = 0.627$  and  $n_{\text{eff}} = 1.25$ , consistent with 25% electron doping.

By contrast, for  $J_K \geq 5$ , we find Fermi points only at  $(\frac{\pi}{2}, 0)$ . For  $k_y = \pm \frac{\pi}{2}, \pi$ , we have to consult  $\rho_{k_y}(\alpha)$  shown in Fig. S-11(b) (green squares and red diamonds). Since these are well below 2, we define  $k_{Fx} = 0$  for these, so that  $(|k_{Fx}|, |k_y|) = (0, \frac{\pi}{2})$  and  $(0, \pi)$ . Insertion into Eq. (S13) yields  $v_{FS} = 0.125$  and  $n_{\text{eff}} = 0.25 = 2.25 \bmod 2$  ( $n_{\text{eff}}$  is only defined modulo 2, i.e. up to filled bands). This is consistent with spins becoming mobile charge carriers by “binding” to the electrons [43] by forming collective Kondo singlets. These collective Kondo singlets break up when approaching the KB-QCP from  $J_K > J_{K,c}$  (hence the name “Kondo breakdown”) and cease to exist for  $J_K < J_{K,c}$ . The existence of collective Kondo singlets manifests in a pole in the single-electron self-energy. Due to this pole, the Fermi wavevector is shifted, leading to a FS consistent with spins counting as mobile charge carriers [42, 43].